ARTICLE

Molecular underpinning of intracellular pH regulation on TMEM16F

Pengfei Liang[1] and Huanghe Yang[1,2]

TMEM16F, a dual-function phospholipid scramblase and ion channel, is important in blood coagulation, skeleton development, HIV infection, and cell fusion. Despite advances in understanding its structure and activation mechanism, how TMEM16F is regulated by intracellular factors remains largely elusive. Here we report that TMEM16F lipid scrambling and ion channel activities are strongly influenced by intracellular pH (pH_i). We found that low pH_i attenuates, whereas high pH_i potentiates, TMEM16F channel and scramblase activation under physiological concentrations of intracellular Ca^{2+} ($[Ca^{2+}]_i$). We further demonstrate that TMEM16F pH_i sensitivity depends on $[Ca^{2+}]_i$ and exhibits a bell-shaped relationship with $[Ca^{2+}]_i$: TMEM16F channel activation becomes increasingly pH_i sensitive from resting $[Ca^{2+}]_i$ to micromolar $[Ca^{2+}]_i$, but when $[Ca^{2+}]_i$ increases beyond 15 μM, pH_i sensitivity gradually diminishes. The mutation of a Ca^{2+}-binding residue that markedly reduces TMEM16F Ca^{2+} sensitivity (E667Q) maintains the bell-shaped relationship between pH_i sensitivity and Ca^{2+} but causes a dramatic shift of the peak $[Ca^{2+}]_i$ from 15 μM to 3 mM. Our biophysical characterizations thus pinpoint that the pH_i regulatory effects on TMEM16F stem from the competition between Ca^{2+} and protons for the primary Ca^{2+}-binding residues in the pore. Within the physiological $[Ca^{2+}]_i$ range, the protonation state of the primary Ca^{2+}-binding sites influences Ca^{2+} binding and regulates TMEM16F activation. Our findings thus uncover a regulatory mechanism of TMEM16F by pH_i and shine light on our understanding of the pathophysiological roles of TMEM16F in diseases with dysregulated pH_i, including cancer.

Introduction

The mammalian TMEM16 family consists of 10 members. TMEM16A and TMEM16B are Ca^{2+}-activated Cl^- channels (CaCCs), which participate in fluid secretion, smooth muscle contraction, gut motility, nociception, motor learning, anxiety, and cancer (Hartzell et al., 2005; Caputo et al., 2008; Yang et al., 2008; Schroeder et al., 2008; Berg et al., 2012; Cho et al., 2012; Huang et al., 2012; Pedemonte and Galietta, 2014; Oh and Jung, 2016; Whitlock and Hartzell, 2017; Zhang et al., 2017; Crottès and Jan, 2019; Li et al., 2019). The majority of the other TMEM16 members are likely not CaCCs (Suzuki et al., 2010; Yang et al., 2012; Huang et al., 2013; Suzuki et al., 2014; Whitlock et al., 2018; Bushell et al., 2019). As one of the most studied TMEM16 proteins, TMEM16F is a dual-function, Ca^{2+}-activated, nonselective ion channel and Ca^{2+}-activated phospholipid scramblase (CaPLSase) that mediates phospholipid flip-flop across membrane lipid bilayers and rapidly destroys the asymmetric distribution of phospholipids on cell membranes (Suzuki et al., 2010; Yang et al., 2012). TMEM16F-mediated cell surface exposure of phosphatidylserine (PS), an amino-phospholipid concentrated in the inner leaflet of the plasma membrane, is essential for a number of cellular and physiological processes,

including blood coagulation (Suzuki et al., 2010; Yang et al., 2012), skeleton development (Ehlen et al., 2013; Ousingsawat et al., 2015), viral infection (Zaitseva et al., 2017), membrane microparticle release (Fujii et al., 2015), cell–cell fusion, and placental development (Zhang et al., 2020). The loss-of-function mutations of human *TMEM16F* cause Scott syndrome, a mild bleeding disorder characterized by a deficiency in CaPLSase-mediated PS exposure and subsequent defects on prothrombinase assembly, thrombin generation, and blood coagulation (Suzuki et al., 2010; Castoldi et al., 2011). Conversely, TMEM16F-deficient mice resist thrombotic challenges, suggesting that TMEM16F CaPLSase has the potential to serve as a promising therapeutic target for thrombotic disorders such as stroke, deep vein thrombosis, and heart attack (Yang et al., 2012). Given its importance in health and disease, it is thus urgent to understand the molecular mechanisms and cellular functions of TMEM16F.

Recent structural and functional studies have advanced our understanding of the molecular architecture and the activation mechanism of TMEM16 CaPLSases (Pedemonte and Galietta, 2014; Brunner et al., 2016; Whitlock and Hartzell, 2017; Falzone et al., 2018). The pore-gate domain of TMEM16 proteins

[1]Department of Biochemistry, Duke University Medical Center, Durham, NC; [2]Department of Neurobiology, Duke University Medical Center, Durham, NC.

Correspondence to Huanghe Yang: huanghe.yang@duke.edu.

consists of not only the permeation pathway for phospholipids and ions, but also two highly conserved Ca^{2+} binding sites (Yu et al., 2012; Brunner et al., 2014; Tien et al., 2014). Binding of intracellular Ca^{2+} triggers conformational changes, which lead to the opening of the activation gates and subsequent lipid and ion permeation (Dang et al., 2017; Paulino et al., 2017; Alvadia et al., 2019; Bushell et al., 2019; Feng et al., 2019; Le et al., 2019b). In addition to intracellular Ca^{2+} concentration ($[Ca^{2+}]_i$), membrane depolarization can also facilitate the activation of TMEM16 CaCCs and TMEM16F ion channels (Caputo et al., 2008; Schroeder et al., 2008; Yang et al., 2008, 2012). In contrast to the comprehensive understanding of their activation mechanisms, the regulatory mechanisms of TMEM16 proteins has just begun to emerge.

Phosphatidylinositol (4,5)-bisphosphate (PIP_2) was recently shown to play a critical role in regulating TMEM16A and TMEM16F ion channel rundown or desensitization (Ta et al., 2017; De Jesús-Pérez et al., 2018; Ye et al., 2018; Le et al., 2019a; Tembo et al., 2019; Yu et al., 2019). In addition, both intracellular and extracellular pH have also been reported to regulate endogenous CaCCs (Arreola et al., 1995; Park and Brown, 1995; Qu and Hartzell, 2000) and heterologous expressed TMEM16A CaCCs (Chun et al., 2015; Cruz-Rangel et al., 2017; Segura-Covarrubias et al., 2020). The Oh laboratory recently reported that intracellular protons can inhibit TMEM16A CaCC by competing with Ca^{2+} on binding to the Ca^{2+} binding sites instead of affecting intracellular histidine residues (Chun et al., 2015). While it was previously reported that TMEM16F channel activity can be modulated by intracellular pH (pH_i; Chun et al., 2015), it is not known whether its phospholipid scrambling activity can also be regulated by pH_i, nor is the mechanism by which pH_i modulates both ion channel and scrambling activities of TMEM16F understood. Interestingly, TMEM16F is highly expressed in various tumor cells including pancreatic ductal adenocarcinoma cells (Wang et al., 2018) and glioma cells (Xuan et al., 2019). Consistent with its high expression levels, TMEM16F has been implicated in tumor cell proliferation, migration, and metastasis (Jacobsen et al., 2013; Wang et al., 2018; Xuan et al., 2019). Given the fact that pH dysregulation (intracellular alkalization to pH_i 7.3–7.6 and extracellular acidification to pH 6.8–7.0) is one of the hallmarks of cancer (Webb et al., 2011; White et al., 2017), it is thus critical to understand whether pH_i can regulate TMEM16F ion channel and CaPLSase activities.

In this study, we used patch-clamp and fluorescence imaging methods to systematically characterize the impacts of pH_i on TMEM16F activation. Our results show that intracellular acidification attenuates, whereas intracellular alkalization potentiates, both TMEM16F ion channel and CaPLSase activities under physiological $[Ca^{2+}]_i$. pH_i mainly affects TMEM16F Ca^{2+}-dependent activation. Our biophysical analysis and mutagenesis studies further demonstrate that the pH_i regulatory effects on TMEM16F stem from the protonation and deprotonation of the Ca^{2+} binding residues, which in turn reduces and enhances Ca^{2+} binding affinity, respectively. Our findings thus uncover a new regulatory mechanism of TMEM16F that will facilitate our understanding of the physiological and pathological functions of

TMEM16F and other TMEM16 family members in health and disease.

Materials and methods
Cell lines and culture
HEK293T cells are authenticated by the Duke Cell Culture Facility. The HEK293T cell line with stable expression of C-terminally eGFP-tagged mTMEM16F has been reported previously (Le et al., 2019b). The TMEM16F-deficient (knockout [KO]) HEK293T cell line was generated using CRISPR-Cas9 and has been validated in our recent studies (Le et al., 2019b, 2019c; Zhang et al., 2020). All our mutagenesis studies were conducted in TMEM16F-KO HEK293T cells. HEK293T cells were cultured with Dulbecco's modified Eagle's medium (DMEM; 11995-065; Gibco BRL) supplemented with 10% FBS (F2442; Sigma-Aldrich) and 1% penicillin–streptomycin (15-140-122; Gibco BRL). All cells were cultured in a humidified atmosphere with 5% CO_2 at 37°C.

Mutagenesis and transfection
The murine TMEM16F (cDNA 6409332; Open Biosystems) and murine TMEM16A (cDNA 30547439; Open Biosystems) coding sequences are in the pEGFP-N1 vector, resulting in eGFP tags on their C termini. Single point mutations were generated using QuikChange site-directed mutagenesis kit (Agilent), and the majority of them have been reported in previous publications. The plasmids were transiently transfected to TMEM16F-KO HEK293T cells using X-tremeGENE9 transfection reagent (Sigma-Aldrich). Cells grown on coverslips coated with poly-L-lysine (Sigma-Aldrich) were placed in a 24-well plate. Medium was changed 6 h after transfection with either regular (11995-065; Gibco BRL) or Ca^{2+}-free (21068-028; Gibco BRL) DMEM. Experiments proceeded 24–48 h after transfection.

Electrophysiology
All currents were recorded in either inside-out or whole-cell configurations 24–48 h after transfection using an Axopatch 200B amplifier (Molecular Devices) and the pClamp software package (Molecular Devices). Glass pipettes were pulled from borosilicate capillaries (Sutter Instruments) and fire-polished using a microforge (Narishge) to reach a resistance of 2–3 MΩ.

For inside-out patch, the pipette solution (external) contained (in mM) 140 NaCl, 10 HEPES, and 1 $MgCl_2$, adjusted to pH 7.3 (NaOH), and the bath solution contained 140 NaCl, 10 HEPES, and 5 EGTA, adjusted to pH 7.3 (NaOH). The zero-Ca^{2+} internal solution contained (in mM) 140 NaCl, 10 HEPES, and 5 EGTA. To avoid the complications in controlling free Ca^{2+} under different pH_i values, Ca^{2+} chelator was excluded from our Ca^{2+}-containing internal solutions. Instead, we directly added $CaCl_2$ into a basal internal solution containing (in mM) 140 NaCl and 10 HEPES, in the absence of Ca^{2+} chelator. We may have underestimated the free Ca^{2+} concentrations in the internal solutions, as there is a minimal amount of contaminating Ca^{2+} from the double-distilled water and the reagents. However, the contaminating Ca^{2+} in our basal solution is very low (<0.5 μM, as estimated by measuring the basal solution-induced TMEM16A-CaCC activation and fitting with a TMEM16A-CaCC dose–response curve that was

constructed by Fura-2 calibrated Ca^{2+} solutions; Le et al., 2019a). As the contaminating Ca^{2+} level is low and exists in all of the pH_i solutions, our conclusions were not affected. Different pH levels were adjusted with either NaOH or HCl as needed.

For whole-cell recordings, the pipette solution (internal) contained (in mM) 140 CsCl, 1 $MgCl_2$, and 10 HEPES, plus $CaCl_2$ to obtain the desired free Ca^{2+} concentration. pH was adjusted by either CsOH or HCl as desired. The bath solution contained (in mM) 140 NaCl, 10 HEPES, and 1 $MgCl_2$, adjusted to pH 7.3 (NaOH). Procedures for solution application were as used previously (Le et al., 2019a). Briefly, a perfusion manifold with 100–200-μm tip was packed with eight PE10 tubes. Each tube was under separate valve control (ALA-VM8; ALA Scientific Instruments), and solution was applied from only one PE10 tube at a time onto the excised patches or whole-cell clamped cells. All experiments were at room temperature (22–25°C). All the chemicals for solution preparation were obtained from Sigma-Aldrich.

Phospholipid scrambling fluorometry
Phospholipid scrambling fluorometry was adapted from the method developed by the Hartzell laboratory (Yu et al., 2015). Instead of delivering and detecting current, the glass pipettes under whole-cell configuration were used to achieve precise control of pH_i and Ca^{2+}. Briefly, the cells were seeded and transfected on poly-L-lysine–coated coverslips before the experiments. Glass pipettes were prepared and filled with internal solution as mentioned in the electrophysiology section. After focusing on the cell-surface eGFP signal from the expressed TMEM16F-eGFP, the light filter set was switched to detect Annexin V-CF594 signal (594 nm). Annexin V-CF 594 (29011; Biotium) was diluted at 0.5 μg ml^{-1} with Annexin V (AnV) binding solution (10 mM HEPES, 140 mM NaCl, and 2.5 mM $CaCl_2$, pH 7.4) and then added into the ALA perfusion system as mentioned above. The perfusion manifold was lowered next to the cell to be patched. Once the whole-cell configuration was established, the perfusion valve was simultaneously opened, and Anv solution was flushed to the patch-clamped cell. At the same time, image acquisition started with intervals of 5–10 s.

Data analysis
G-V curves were constructed from tail currents measured 200–400 μs after repolarization. In cases in which the tail currents were tiny, steady-state peak currents were used to build the I-V relation. For the G-V curves obtained from the same patch, the conductance was normalized to the maximal conductance obtained at pH 8.9 and the high depolarization voltage. Individual G-V curves were fitted with a Boltzmann function,

$$G(V) = \frac{G_{max}}{1 + e^{\frac{-ZF(V-V_{0.5})}{RT}}}, \qquad (1)$$

where G_{max} denotes the fitted value for maximal conductance at a given pH, $V_{0.5}$ denotes the voltage of half-maximal activation of conductance, z denotes the net charge moving across the membrane during the transition from the closed to the open state, and F denotes the Faraday constant.

Dose–response curves were fitted with the Hill equation,

$$\frac{G}{G_{max}} = \frac{1}{1 + \frac{[EC_{50}]^H}{[Ca^{2+}]}}, \qquad (2)$$

where G/G_{max} denotes current normalized to the maximum current elicited by 1,000 μM Ca^{2+} at given pH_i, $[Ca^{2+}]$ denotes free Ca^{2+} concentration, H denotes the Hill coefficient, and EC_{50} denotes the half-maximal activation concentration of Ca^{2+}.

Bell-shape fitting of the pH_i sensitivity–$[Ca^{2+}]_i$ relationship was performed with bell-shaped dose–response function of Prism software (GraphPad). Briefly, pH_i sensitivity (Y) and Ca^{2+} concentration (X) were fitted with the following equations:

$$Y = Peak + Section1 + Section2; \qquad (3)$$

$$Section1 = \frac{Span1}{1 + 10^{(logEC_{50\_1}-X)*nH_1}}; \qquad (4)$$

$$Section2 = \frac{Span2}{1 + 10^{(logEC_{50\_2}-X)*nH_2}}; \qquad (5)$$

$$Span1 = Plateau1 - Peak; \qquad (6)$$

$$Span2 = Plateau2 - Peak, \qquad (7)$$

where Plateau1 and Plateau2 denote the plateaus at the left and right ends of the curve, which are set to be 0 in this study; Peak is the maximum value of the curve; X is the Ca^{2+} concentration; $logEC_{50\_1}$ and $logEC_{50\_2}$ are the concentrations that give half-maximal stimulatory and inhibitory effects in the same units as X; and nH_1 and nH_2 are the unitless slope factors or Hill slopes, which are set to be 1 in this study.

PDB coordinate files were downloaded from the Protein Data Bank website (https://www.rcsb.org/). All figures with TMEM16 structures were generated with Pymol software (Schrödinger, Inc.).

Quantifying phospholipid scrambling activity
To analyze the accumulation of AnV fluorescence signal on cell surfaces over time, a previously reported Matlab (Mathworks) code was used (Le et al., 2019b). Briefly, a region of interest was manually chosen around the scrambling cells, and AnV fluorescence intensity was calculated using the following equation for each frame:

$$F = \sum_{n=1}^{N} f, \qquad (8)$$

where f equals the fluorescent intensity of each pixel and N is the number of pixels in the region of interest.

The time-dependent increase of AnV fluorescence was fitted with a generalized logistic equation (Yin et al., 2003):

$$F = \frac{F_{max}}{1 + e^{-k(t-t_{1/2})}}, \qquad (9)$$

where F_{max} is the maximum normalized AnV fluorescence intensity, which is set to 100% in this study; k is the maximum growth rate (or the slope) of the linear phase in the sigmoidal curve; and $t_{1/2}$ is the time point at which the fluorescent intensity reaches half of its maximum value and the fluorescence increase rate reaches its maximum.

Statistical analysis
All statistical analyses were performed with Clampfit 10.7, Excel, and Prism. Two-tailed Student's t test was used for single

comparisons between two groups (paired or unpaired), and one-way ANOVA followed by Tukey's test was used for multiple comparisons. Data are represented as mean ± SEM unless stated otherwise. Symbols denote statistical significance as follows: *, $P < 0.05$; **, $P < 0.01$; ***, $P < 0.001$; ****, $P < 0.0001$; and ns, no significance.

Data availability

We deposited the source data file, all the video files, and the Matlab code used to analyze fluorescence images to Dyrad (https://datadryad.org/stash/dataset/doi:10.5061/dryad.b8gtht79d).

Online supplemental materials

pH_i regulation on TMEM16A is presented in Fig. S1. Fig. S2 shows the TMEM16F current rundown at different pH_i values. Fig. S3 shows the pH_i regulation on a pore-lining residue mutation Q559K. Fig. S4 shows the lipid scrambling activity of TMEM16F-KO HEK239T cells at different pH_i values. Fig. S5 shows the pH_i regulation of TMEM16A at 100 µM Ca^{2+}. Fig. S6 shows the pH_i regulation on TMEM16A and TMEM16F gain-of-function mutations in the absence of intracellular Ca^{2+}. Fig. S7 shows pH_i regulation on a Ca^{2+} binding site near the dimer interface. Table S1 shows the comparison of pH_i sensitivity of TMEM16F current measurements using Boltzmann fit and linear fit. Video 1 shows the lipid scrambling activity of HEK293T cells overexpressing TMEM16F with 100 µM Ca^{2+} at pH_i 6.1, 7.3, and 8.9 (related to Fig. 2 B). Video 2 shows the lipid scrambling activity of TMEM16F-KO HEK293T cells with 100 µM Ca^{2+} at various pH_i values (related to Fig. S4). Video 3 shows the lipid scrambling activity of HEK293T cells overexpressing TMEM16F with 5 µM Ca^{2+} at pH_i 6.1, 7.3, and 8.9 (related to Fig. 4 A). Video 4 shows the lipid scrambling activity of HEK cells overexpressing TMEM16F with 1,000 µM Ca^{2+} at pH_i 6.1, 7.3, and 8.9 (related to Fig. 4 F).

Results

pH_i regulates TMEM16F ion channel activity

We first evaluated the pH_i effect on TMEM16F ion channel activity. Instead of using the gap-free protocol at fixed membrane voltages in a previous study (Chun et al., 2015), we used inside-out patches to measure TMEM16F current activation across a wide range of voltages under different pH_i values so that the G-V relationships can be constructed and the pH_i effects can be compared at different values of pH_i, voltage, and $[Ca^{2+}]_i$. Consistent with the previous report (Chun et al., 2015), our analysis shows that low pH_i (<7.3) greatly suppresses TMEM16F channel activity. In addition, our recordings show that alkalized pH_i (>7.3) greatly potentiates TMEM16F current in a pH_i-dependent fashion compared with a physiological pH_i of 7.3 (Fig. 1, A and B).

The apparent pH_i sensitivity of TMEM16F channel was assessed by plotting the conductance-pH_i (G-pH_i) relationship (Fig. 1 C), which results in a sigmoidal curve and saturates at pH_i 10.6. Under the physiologically relevant pH_i range (6.1–8.9), the linear regression aligned well with the Boltzmann sigmoidal fit, suggesting that at least in this pH_i range, linear regression can be
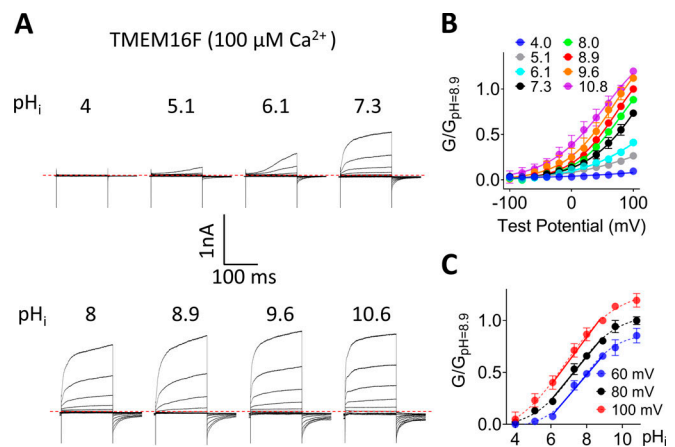

Figure 1. **pH_i regulates TMEM16F ion channel activity. (A)** Representative TMEM16F currents recorded from inside-out patches perfused with intracellular solutions containing 100 µM Ca^{2+} at different pH_i values. Currents were evoked by voltage steps from –100 to +100 mV with 20 mV increments, and the holding potential was –60 mV. All traces shown were from the same patch. **(B)** Mean G-V relations of the TMEM16F channels under different pH_i values at 100 µM Ca^{2+}. Relative conductance was determined by measuring the amplitude of tail currents 400 µs after repolarization to a fixed membrane potential (–60 mV). The smooth curves represent Boltzmann fits $G/G_{max} = 1/\{1 + exp[–ze(V – V_{1/2})/kT]\}$. G_{max} is tail current amplitude in response to depolarization to +100 mV in 100 µM Ca^{2+} at pH_i 8.9. Error bar represents SEM (n = 7). **(C)** G-pH_i relationship for TMEM16F channels. Data were normalized to pH_i 8.9. Dashed line represents Boltzmann fit. G-pH_i curves from 6.1 to 8.9 were fitted with linear regression shown as the solid lines, which aligned well with the Boltzmann fits (dashed line). Thus, the mean slopes from linear regression were used as a parameter for pH_i sensitivity in later experiments (n = 7).

used to assess the pH_i sensitivity of TMEM16F (Table S1). Moreover, our results reveal that TMEM16F pH_i sensitivity is voltage independent as evidenced by the parallel G-pH_i relationships at different voltages (Fig. 1 C). To further validate our measurements and quantification, we characterized the pH_i effects on TMEM16A at different membrane voltages (Fig. S1). Consistent with the previous report (Chun et al., 2015), our analysis also shows that low pH_i (6.1) greatly suppresses, whereas high pH_i (8.9) significantly potentiates, TMEM16A activation in the presence of 0.5 µM $[Ca^{2+}]_i$, as evidenced by the dramatic leftward and rightward shifts of the G-V curves, respectively (Fig. S1, A and B). Similar to pH_i's effect on TMEM16F, the G-pH_i relation of TMEM16A also exhibited a linear relation within the pH_i range tested (6.1–8.9; Fig. S1 C). The almost identical slopes of the G-pH_i plots under different membrane potentials suggest that pH_i has negligible effect on TMEM16A voltage-dependent activation, which again resembles what we observed in TMEM16F (Fig. 1 C). Taken together, our patch clamp recordings reveal that pH_i is an important intracellular factor to regulate both TMEM16A and TMEM16F ion channel activities.

As TMEM16F channel activity is subject to PIP_2-dependent rundown or desensitization under inside-out configuration (Ye et al., 2018), we then estimated the influence of rundown on our quantification of pH_i sensitivity. As shown in Fig. S2, A and B, the peak currents elicited by a voltage-step protocol reduced

only <20% under all pH_i values tested within the time window to complete all the recordings shown in Fig. 1 A (~1 min), suggesting that TMEM16F current rundown does not exert a dramatic impact on our measurements. To further reduce the influence of TMEM16F current rundown on our quantifications, we sequentially perfused different pH_i solutions from low pH_i to high pH_i and then normalized all TMEM16F current to the maximum current at pH_i 10.6, which was applied last (Fig. 1 C). If taking channel rundown into account, the pH_i sensitivity of TMEM16F channel in our measurements would have been underestimated. To further validate our pH_i sensitivity quantification, we measured the pH_i sensitivity of Q559K (Fig. S3), a pore-lining residue mutation that shows no current rundown (Ye et al., 2018). We found that Q559K and WT TMEM16F show nearly identical pH_i sensitivity (0.20 ± 0.02 and 0.22 ± 0.04, respectively) under 100 µM $[Ca^{2+}]_i$ and +100 mV (Fig. S3 C). This experiment further demonstrated that TMEM16F current rundown has a negligible effect on our pH_i sensitivity quantifications.

pH_i regulates TMEM16F scrambling activity

Having shown that pH_i can regulate TMEM16F ion channel activity, we next sought to examine whether pH_i can also influence TMEM16F lipid scrambling activity. To quantify TMEM16F lipid scrambling at different pH_i values, we used the patch clamping–lipid scrambling fluorometry dual recording assay (Yu et al., 2015) to overcome the difficulties in precisely controlling pH_i and $[Ca^{2+}]_i$ (Fig. 2 A). In this assay, pH_i and $[Ca^{2+}]_i$ are accurately controlled by solution exchange between glass pipettes and the cytosol of the whole-cell patch clamped cells. Once TMEM16F is activated by $[Ca^{2+}]_i$, AnV starts to be attracted to the cell surface by the externalized PS, after a delay (Fig. 2 B and Video 1). The fluorescence signal accumulated on the cell surface increases over time and exhibits a sigmoid relationship with time (Fig. 2 C). At physiological pH_i of 7.3, 100 µM $[Ca^{2+}]_i$ activates TMEM16F lipid scramblases with an average onset time (t_{on}) of 11.3 min (Fig. 2 D), which is comparable with previous reports (Grubb et al., 2013; Yu et al., 2015). We found that intracellular alkalization (pH_i 8.9) markedly shortened t_{on} to ~4.5 min. In stark contrast, intracellular acidification (pH_i 6.1) significantly prolonged t_{on} to 18.3 min. By fitting the curve with a generalized logistic function, we can obtain $t_{1/2}$, the time needed to reach half-maximum fluorescence when the macroscopic CaPLSase activity reaches maximum speed. At physiological pH_i of 7.3, 100 µM $[Ca^{2+}]_i$ activates TMEM16F lipid scramblases with an average $t_{1/2}$ of 20.3 min (Fig. 2 E). We found that intracellular alkalization (pH_i 8.9) markedly shortened $t_{1/2}$ to ~11.6 min. In stark contrast, intracellular acidification (pH_i 6.1) significantly prolonged $t_{1/2}$ to 29.1 min. The changes of $t_{1/2}$ under different pH_i values indicate that low pH_i attenuates, and high pH_i enhances, TMEM16F CaPLSase activities. We also quantified the maximum lipid scrambling rate at $t_{1/2}$, or the slope (k) of the linear phase on the sigmoid curves under different pH_i values. We found that low pH_i (6.1) significantly reduced slope k from 0.26 at physiological pH_i to 0.19, whereas high pH_i (8.9) increased slope k to 0.4 (Fig. 2 F), suggesting that pH_i affects the maximum lipid scrambling rate of TMEM16F.

To ensure that enhanced PS externalization at high pH_i is mediated by TMEM16F CaPLSases instead of other mechanisms such as alkalization-induced apoptosis (Lagadic-Gossmann et al., 2004), we used the patch-fluorometry assay to measure our TMEM16F KO HEK293T cells, which lack endogenous CaPLSase activity (Le et al., 2019c), at pH_i values ranging from 6.1 to 8.9. In stark contrast to fast lipid scrambling in TMEM16F-stable HEK293T cells (Fig. 2 C), we did not observe any obvious AnV binding to the TMEM16F KO cells over 25–40 min (Fig. S4 and Video 2). This experiment suggests that apoptosis-induced PS exposure is unlikely to contribute to the pH_i effects on TMEM16F CaPLSases under our experimental conditions.

In summary, our patch lipid scrambling–fluorometry measurement demonstrated that TMEM16F CaPLSase activity is also regulated by pH_i. By carefully quantifying the effects of pH_i on TMEM16F CaPLSase activity, we obtained three parameters, t_{on}, $t_{1/2}$, and slope k, to evaluate CaPLSase activity (see Discussion for detailed explanation on the physical meaning of these parameters). The changes of the three parameters under different pH_i values explicitly demonstrate that TMEM16F CaPLSase activity (Fig. 2), similar to its ion channel activity (Fig. 1, A–C), is highly sensitive to pH_i regulation. Under physiological pH_i, intracellular acidification suppresses TMEM16F CaPLSase and ion channel activation, whereas intracellular alkalization enhances TMEM16F activation. This implies that the pH_i effects on TMEM16F ion channel and lipid scrambling might share the same molecular mechanism.

pH_i regulation of TMEM16F ion channel activity is Ca^{2+} dependent

As lowering pH_i has been reported to inhibit Ca^{2+}-dependent activation of TMEM16A (Chun et al., 2015), we next examined whether pH_i's effect on TMEM16F channel activation is also through influencing its Ca^{2+} dependence, by comparing the pH_i effects under 5, 100, and 1,000 µM $[Ca^{2+}]_i$. Under 5 µM $[Ca^{2+}]_i$, TMEM16F channel activation is strongly pH_i dependent (Fig. 3, A and C). The apparent pH_i sensitivity at 100 mV under 5 µM $[Ca^{2+}]_i$ increases to ~0.32 compared with 0.22 under 100 µM $[Ca^{2+}]_i$, suggesting that TMEM16F pH_i sensitivity is enhanced when $[Ca^{2+}]_i$ is low (Fig. 3 E). In contrast, the pH_i effect is almost completely diminished when $[Ca^{2+}]_i$ is increased to 1,000 µM, as seen by the robust and almost identical activation of TMEM16F current from pH_i 6.1 to 8.9 and nearly flat G-pH_i relationships (Fig. 3, B, D, and E). Consistently, when saturating $[Ca^{2+}]_i$ (100 µM) was applied to TMEM16A-CaCC at different pH_i values, the pH_i effect on TMEM16A also diminished (Fig. S5). Our results thus demonstrate that the pH_i regulation of TMEM16F and TMEM16A channel is highly Ca^{2+} dependent: lower $[Ca^{2+}]_i$ enhances pH_i sensitivity, whereas saturating $[Ca^{2+}]_i$ (1,000 µM for TMEM16F and 100 µM for TMEM16A) eliminates pH_i sensitivity.

TMEM16F channel activation requires both $[Ca^{2+}]_i$ and membrane depolarization (Yang et al., 2012). To assess the influence of pH_i on voltage-dependent activation, we examined the gain-of-function mutations in the pore—namely TMEM16A-Q645A, TMEM16A-L543Q (Fig. S6 A), TMEM16F-F518K, and
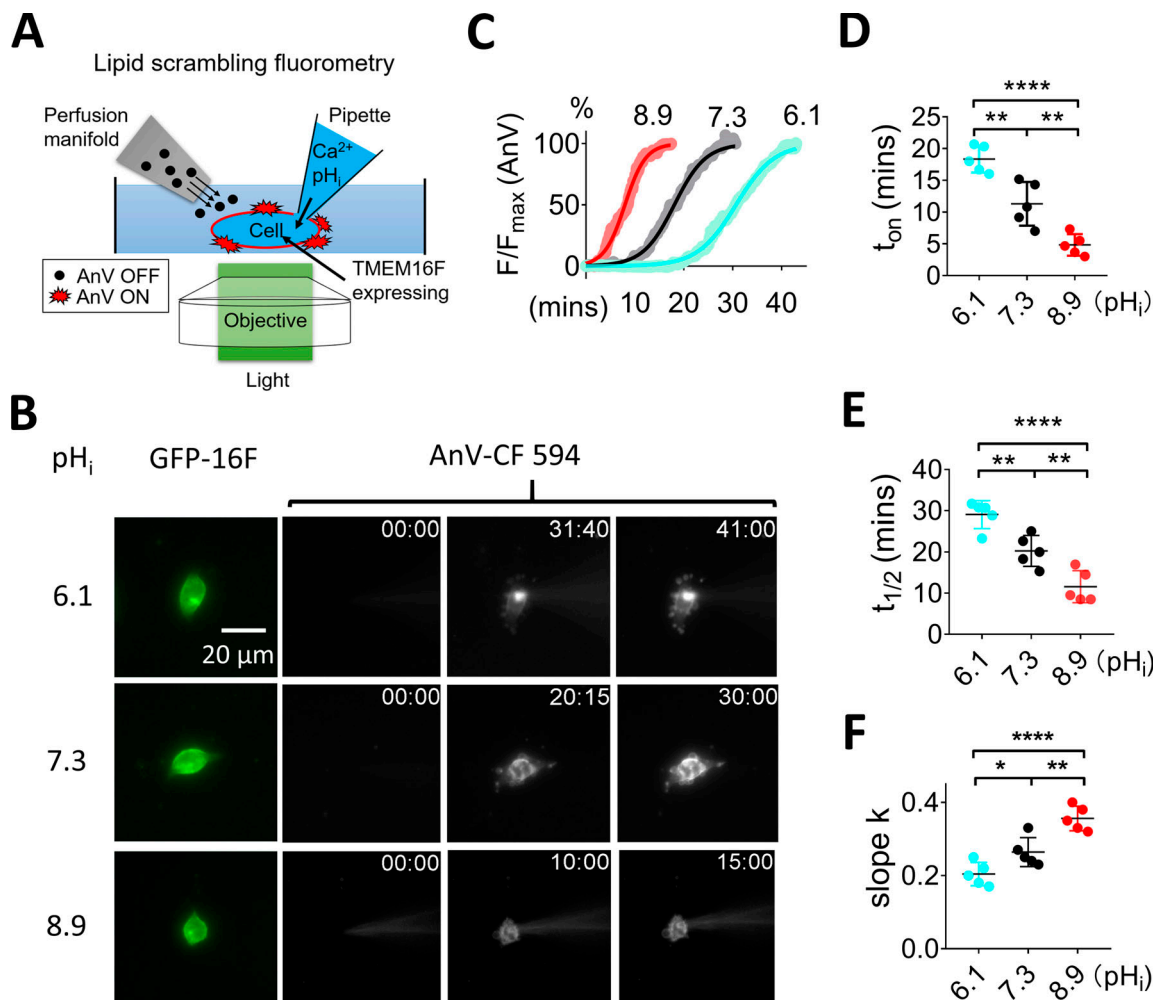
Figure 2. **pH$_i$ regulates TMEM16F lipid scrambling activity. (A)** Schematic design of the lipid scrambling fluorometry assay. CaPLSase activity is monitored by cell-surface accumulation of fluorescently tagged AnV, a PS binding protein that is continuously perfused through a perfusion manifold. AnV fluorescence remains dim in bulk solution and will strongly fluoresce after being recruited by cell surface PS, which is externalized by CaPLSases. We use whole-cell patch pipettes to deliver intracellular solutions into the cytosol to achieve precise control of pH$_i$ and Ca^{2+}. Once breaking into whole-cell configuration, the pipette solution rapidly diffuses into the cell and activates CaPLSases. AnV fluorescence signal on the cell surface was continuously recorded with 5-s intervals. **(B)** Representative lipid scrambling fluorometry images of HEK293T cells stably expressed with TMEM16F-eGFP (left, green signal) at different pH$_i$ values. For the AnV-CF 594 signal on the right, the first column is fluorescence signal immediately after forming whole-cell configuration; the second column is the time when fluorescence intensity reached half maximum ($t_{1/2}$), and the last column is the time when fluorescence signal reached roughly plateau. The time points (minutes followed by seconds) of each image after breaking into whole-cell configuration are shown on the top right corner. The pipette solution contained 100 µM Ca^{2+}, and holding potential was −60 mV. See also Video 1. **(C)** The time course of AnV fluorescence signal at different pH$_i$ values as shown in B. The AnV signal was normalized to the maximum AnV fluorescence intensity at the end of each recording. The smooth curves represent fits to generalized logistic equation, $F = F_{max}/\{1 + \exp[-k(t - t_{1/2})]\}$. **(D)** Under 100 µM Ca^{2+}, the onset times (t_{on}), when AnV signal can be reliably detected, for pH$_i$ 6.1, 7.3, and 8.9 are 18.3 ± 1.3 (n = 5), 11.3 ± 1.4 (n = 5), and 4.5 ± 0.7 min (n = 5), respectively. **(E)** Under 100 µM Ca^{2+}, $t_{1/2}$ values for pH$_i$ 6.1, 7.3, and 8.9 are 29.07 ± 1.35, 20.28 ± 1.51, and 11.59 ± 1.56 min (n = 5), respectively. **(F)** Under 100 µM Ca^{2+}, slopes for pH$_i$ 6.1, 7.3, and 8.9 are 0.19 ± 0.01, 0.26 ± 0.02, and 0.40 ± 0.02 (n = 5), respectively. Values represent mean ± SEM. *, P < 0.05; **, P < 0.01; ****, P < 0.0001, using one-way ANOVA followed by Tukey's test.

TMEM16F-Y563K (Fig. S6 D; Peters et al., 2018; Le et al., 2019b)—whose opening can be activated solely by membrane depolarization (Fig. S6, B and E). Our results show that in the absence of Ca^{2+}, the pH$_i$ effects on the gain-of-function TMEM16A (Fig. S6, B and C) and TMEM16F mutant channels (Fig. S6, E and F) are almost entirely abolished, as evidenced by the nearly flat *I-pH$_i$* curves for all the gain-of-function mutations (Fig. S6, C and F). Taken together, our biophysical characterizations showed that pH$_i$ specifically regulates the Ca^{2+}-dependent activation of TMEM16A and TMEM16F ion channels.

pH$_i$ regulation of TMEM16F lipid scrambling activity is Ca^{2+} dependent

We next addressed whether the pH$_i$ regulation on TMEM16F lipid scrambling is also [Ca^{2+}]$_i$ dependent, using the patch-lipid scrambling fluorometry assay (Fig. 2 A). Under 5 µM [Ca^{2+}]$_i$, TMEM16F lipid scrambling is strongly pH$_i$ dependent (Fig. 4, A and B; and Video 3). However, compared with 100 µM [Ca^{2+}]$_i$, t_{on} and $t_{1/2}$ under 5 µM [Ca^{2+}]$_i$ are significantly delayed at pH$_i$ 7.3 and 8.9 (Fig. 4, C and D). In addition, the maximum lipid scrambling rates as quantified by slope k are significantly reduced under 5 µM [Ca^{2+}]$_i$ compared with 100 µM [Ca^{2+}]$_i$ (Fig. 4
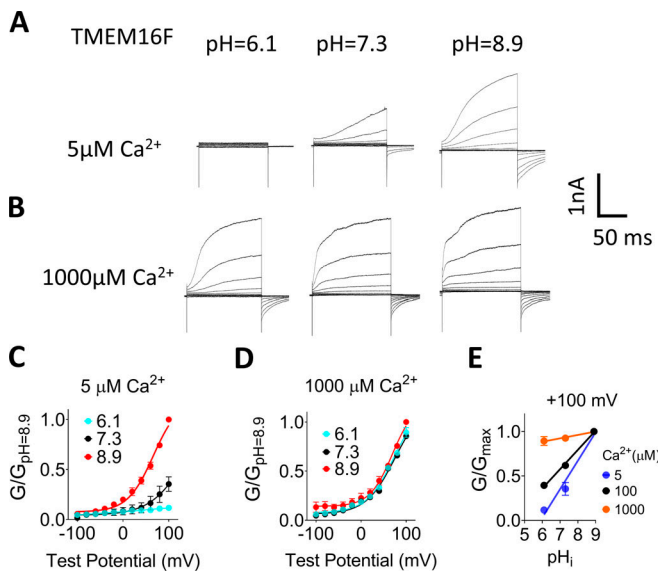
Figure 3. **pH_i regulation of TMEM16F channel activity is Ca²⁺ dependent. (A and B)** Representative TMEM16F currents recorded from inside-out patches perfused with intracellular solutions containing 5 and 1,000 μM Ca²⁺, respectively. All traces shown in each panel were from the same patch. Currents were elicited by voltage steps from −100 to +100 mV with 20-mV increments. The holding potential was −60 mV. **(C and D)** Mean G-V relations of the TMEM16F currents from A and B, respectively. Relative conductance was determined by measuring the amplitude of tail currents 400 μs after repolarization to a fixed membrane potential (−60 mV). The smooth curves represent Boltzmann fits. Error bars represent SEM ($n = 5$). **(E)** pH_i sensitivity of TMEM16F current at +100 mV was measured by the slope of the the G-pH_i relationship. Mean conductance at different Ca²⁺ concentrations was normalized to the maximum conductance at pH_i 8.9 and +100 mV. Averaged slopes from linear fit for 5 and 1,000 μM Ca²⁺ were 0.32 and 0.04, respectively. The G-pH_i curve at 100 μM Ca²⁺ was replotted as black line for reference. Error bars represent SD ($n = 5$).

E). TMEM16F scrambling activity under 5 μM $[Ca^{2+}]_i$ is completely abolished under pH_i 6.1. This is distinct from TMEM16F scrambling in 100 μM $[Ca^{2+}]_i$ and pH_i 6.1, under which condition TMEM16F-mediated lipid scrambling can be clearly observed (Fig. 2, B–E). In contrast, when saturated intracellular Ca²⁺ (1,000 μM) was applied, fast and robust PS exposure could be detected at all pH_i values (Fig. 4 F and Video 4). In addition, the t_{on}, $t_{1/2}$, and maximum lipid scrambling rates (slope k) of TMEM16F lipid scrambling are comparable regardless of pH_i (Fig. 4, H–J). Our imaging experiments thus demonstrate that, consistent with TMEM16F channel activity (Fig. 3), pH_i regulation of TMEM16F CaPLSase activity is also highly $[Ca^{2+}]_i$ dependent: lower $[Ca^{2+}]_i$ enhances TMEM16F CaPLSase pH_i sensitivity, whereas saturating 1,000 μM $[Ca^{2+}]_i$ eliminates its pH_i sensitivity.

pH_i alters Ca²⁺ sensitivity of TMEM16F ion channel

Having shown that pH_i regulation of TMEM16F is $[Ca^{2+}]_i$ dependent (Figs. 3 and 4) yet voltage independent (Fig. 1 C), we next tested the hypothesis that pH_i may directly influence the Ca²⁺ binding sites of TMEM16F, following the same pH_i regulation mechanism of TMEM16A (Chun et al., 2015). If this is the case, protonation and deprotonation of the Ca²⁺ binding residues

would reduce and increase the Ca²⁺ sensitivity of TMEM16F, respectively. To test this hypothesis, we measured the apparent Ca²⁺ sensitivity of TMEM16F under different pH_i values using inside-out patches (Fig. 5 A). Our results showed that the EC₅₀ of the TMEM16F Ca²⁺ dose response under physiological pH_i (7.3) is 6.20 ± 0.82 μM (Fig. 5, B and C), comparable to previous studies (Yang et al., 2012). When pH_i drops to 6.1, TMEM16F Ca²⁺ sensitivity decreases >20-fold (EC₅₀ = 144.45 ± 6.80 μM). In stark contrast, when pH_i is switched to 8.9, TMEM16F Ca²⁺ sensitivity is dramatically enhanced (EC₅₀ = 1.24 ± 0.14 μM). These results support that pH_i works on the Ca²⁺ binding sites to exert its regulatory effects.

Next, we extracted the relative conductance (G/G_{max}) from Fig. 5 B and plotted the G-pH_i relationship for each $[Ca^{2+}]_i$ value (Fig. 5 D). The G-pH_i relationships under different $[Ca^{2+}]_i$ values are not parallel, which is in stark contrast to the parallel G-pH_i relationships under different membrane voltages (Fig. 1 C). As the slope of the G-pH_i relationship represents the apparent pH_i sensitivity, we constructed the pH_i sensitivity–$[Ca^{2+}]_i$ relationship in Fig. 5 E. Interestingly, the pH_i sensitivity–$[Ca^{2+}]_i$ curve displays a bell-shaped distribution, which peaks around 15 μM $[Ca^{2+}]_i$. Recapitulating the bell-shaped Ca²⁺ response curves of inositol (1,4,5)-trisphosphate and Ca²⁺-gated inositol (1,4,5)-trisphosphate receptor, and ryanodine receptor channels (Bezprozvanny et al., 1991), the bell-shaped pH_i sensitivity–$[Ca^{2+}]_i$ curve of TMEM16F demonstrates that TMEM16F is strictly pH_i sensitive under the physiological range of $[Ca^{2+}]_i$. TMEM16F channel activation becomes more and more sensitive to pH_i when $[Ca^{2+}]_i$ elevates from resting levels of 0.1 μM, until its pH_i sensitivity peaks around 15 μM $[Ca^{2+}]_i$. When $[Ca^{2+}]_i$ increases beyond 15 μM $[Ca^{2+}]_i$, TMEM16F pH_i sensitivity sharply decreases. Our analysis thus defines the physiological $[Ca^{2+}]_i$ range for TMEM16F pH_i regulation. In addition, the bell-shaped pH_i sensitivity–$[Ca^{2+}]_i$ curve also suggests that proton and Ca²⁺ compete to bind to the Ca²⁺ binding site residues. When $[Ca^{2+}]_i$ is low, the protonation state of the Ca²⁺ binding residues has a bigger influence on controlling Ca²⁺ binding; thus TMEM16F has higher pH_i sensitivity. When $[Ca^{2+}]_i$ increases beyond 15 μM, Ca²⁺ outcompetes protons to bind to the Ca²⁺ binding residues, thereby resulting in pH_i sensitivity reduction. Once $[Ca^{2+}]_i$ reaches a saturating concentration of 1 mM, TMEM16F can be fully activated even in low pH_i, thereby completely losing pH_i sensitivity.

The primary Ca²⁺ binding sites in the pore mediate pH_i regulation on TMEM16F

To further test this hypothesis and to prove that pH_i directly affects the primary Ca²⁺ binding sites within the pore, we examined the pH_i sensitivity of E667Q, the Ca²⁺ binding residue mutation that markedly reduces TMEM16F Ca²⁺ sensitivity, with an EC₅₀ of 2.8 mM (Yang et al., 2012). Similar to WT TMEM16F, E667Q activation is also highly pH_i dependent, albeit at greatly reduced Ca²⁺ sensitivity in the millimolar range (Fig. 6, A–C). The EC₅₀ of E667Q at pH_i 6.1, 7.3, and 8.9 is 8.8, 3.6, and 1.3 mM, respectively, indicating that pH_i still can regulate TMEM16F Ca²⁺-dependent activation even when the Ca²⁺ binding sites are disrupted. By plotting the G-pH_i relationship and extracting pH_i
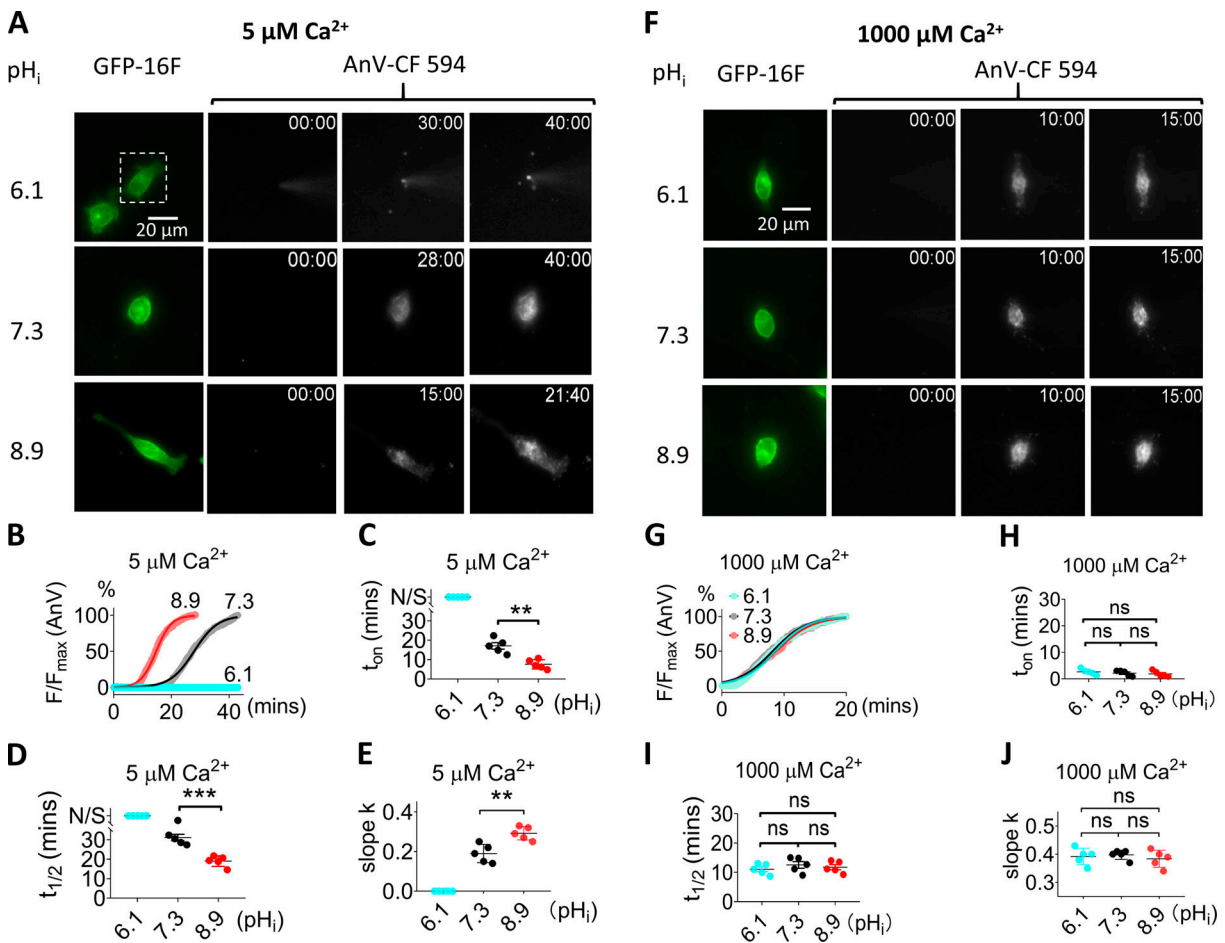
Figure 4. **pH$_i$ regulation of TMEM16F scrambling activity is Ca^{2+} dependent. (A)** Representative images of TMEM16F-eGFP scrambling activity under 5 µM intracellular Ca^{2+} with different pH$_i$ values. The white dotted rectangles in the top row demarcate the patch-clamped TMEM16F-eGFP–expressing cells. For the AnV-CF 594 signals on the right, the first column is fluorescence signal immediately after forming whole-cell configuration; the second column is the time point (minutes followed by seconds, top right corner) when fluorescence intensity reaches half maximum ($t_{1/2}$), and the last column is the time point when fluorescence reaches plateau. No obvious AnV-CF 594 signal can be detected in pH$_i$ 6.1 over 40 min. The recording interval is 10 s. See also Video 3. **(B)** The time courses of AnV fluorescence intensity for TMEM16F activated by 5 µM Ca^{2+} under different pH$_i$ values in A. The smooth curves represent fits to the logistic equation similar to Fig. 2 B. **(C)** The scrambling onset time (t_{on}) at different pH$_i$ values under 5 µM Ca^{2+}. N/S at pH$_i$ = 6.1 represents no scrambling. Error bars represent SEM (n = 5). **(D)** The $t_{1/2}$ at different pH$_i$ values under 5 µM Ca^{2+}. N/S at pH$_i$ = 6.1 represents no scrambling. Error bars represent SEM (n = 5). **(E)** The slopes at different pH$_i$ values under 5 µM Ca^{2+}. **(F)** Representative images of TMEM16F-eGFP scrambling activity under 1,000 µM intracellular Ca^{2+} with different pH$_i$. For the AnV-CF 594 signal on the right, the first column is fluorescence signal immediately after forming whole-cell configuration; the second column is the time point when fluorescence intensity reaches half maximum ($t_{1/2}$), and the last column is the time point when fluorescence reaches plateau. See also Video 4. **(G)** Time courses of AnV fluorescence intensity for TMEM16F activated by 1,000 µM Ca^{2+} under diff,erent pH$_i$ values in F. The smooth curves represent fits to the logistic equation. **(H)** The scrambling onset time (t_{on}) at different pH$_i$ values under 1,000 µM Ca^{2+}. Error bars represent SEM (n = 5). **(I)** The $t_{1/2}$ of lipid scrambling at different pH$_i$ values under 1,000 µM Ca^{2+}. **(J)** The slopes (k) at different pH$_i$ values under 1,000 µM Ca^{2+}. Error bars represent SEM (n = 5). Statistics were analyzed using one-way ANOVA followed by Tukey's test. **, P < 0.01; ***, P < 0.001; ns (not significant), P > 0.05.

sensitivity for each [Ca^{2+}]$_i$ (Fig. 6 D), we constructed the pH$_i$ sensitivity–[Ca^{2+}]$_i$ curve for E667Q (Fig. 6 E). Interestingly, the pH$_i$ sensitivity–[Ca^{2+}]$_i$ curve still displays a bell-shaped distribution, with a significant rightward shift, which peaks around 3.0 mM [Ca^{2+}]$_i$. E667Q shows prominent pH$_i$ sensitivity of 0.15 at 1 mM Ca^{2+}, at which WT TMEM16F completely loses pH$_i$ sensitivity (Fig. 6, D and E). When [Ca^{2+}]$_i$ increases beyond 3 mM, the pH$_i$ sensitivity of E667Q starts to diminish, and it completely loses pH$_i$ sensitivity when [Ca^{2+}]$_i$ reaches saturating 20 mM. As E667Q still requires Ca^{2+} binding to the primary Ca^{2+} binding sites to be activated, our findings in E667Q thus further support that protons and [Ca^{2+}]$_i$ compete to bind to the primary

Ca^{2+} binding sites to control TMEM16F activation. In addition, the pH$_i$ sensitivity at the peak of the pH$_i$ sensitivity–[Ca^{2+}]$_i$ curve of E667Q (0.22) is lower than that of WT channels (0.32). The pH$_i$ sensitivity–[Ca^{2+}]$_i$ curve of E667Q also becomes narrower. All of these results indicate that overall pH$_i$ sensitivity is reduced when the primary Ca^{2+} binding sites are partially disrupted (Fig. 6 E).

Recent structural studies demonstrated that mammalian TMEM16 proteins may possess an additional Ca^{2+} binding site (or the third Ca^{2+} binding site) located near the dimer interface (Alvadia et al., 2019; Bushell et al., 2019). To examine if the putative third Ca^{2+} binding site involves pH$_i$ regulation, we
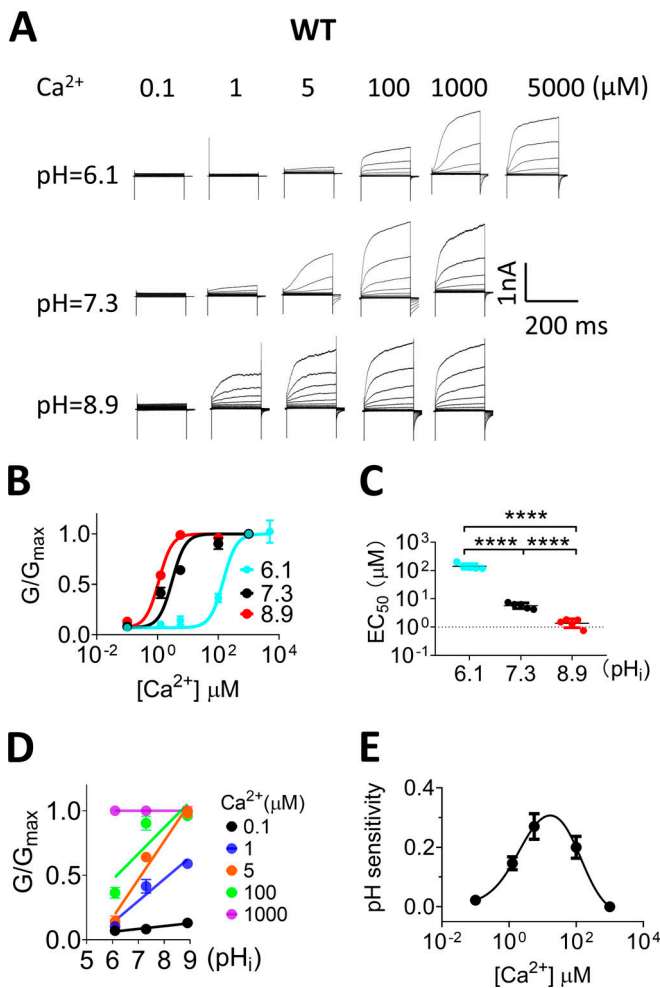
Figure 5. **pH$_i$ alters Ca^{2+} binding affinity of TMEM16F. (A)** Representative TMEM16F currents recorded from inside-out patches perfused with intracellular solutions containing 0.1, 1, 5, 100, 1,000, and 5,000 µM Ca^{2+} at different pH$_i$ values (5,000 µM at pH 6.1 only). **(B)** Ca^{2+} dose–response of mTMEM16F channel at +100 mV with different pH$_i$ values. The smooth curves represent the fits to the Hill equation: $G/G_{max} = G_{1,000}/[1 + (K_d/[Ca^{2+}])^H]$, where K_d is the apparent dissociation constant, H is the Hill coefficient, and $G_{1,000}$ is the conductance with 1,000 µM Ca^{2+} at given pH$_i$. The error bars represent SEM (n = 5). **(C)** EC$_{50}$ values of Ca^{2+} at pH$_i$ 6.1, 7.3 and 8.9 were 144.45 ± 6.80, 6.20 ± 0.82, and 1.24 ± 0.14 µM, respectively. The error bars represent SEM (n = 5). P values were determined with Tukey test comparisons after one-way ANOVA: ****, P < 0.0001. **(D)** The G-pH$_i$ relationship of TMEM16F current at +100 mV under different Ca^{2+} concentrations. Solid lines represent linear fits. **(E)** The relationship of pH$_i$ sensitivity and [Ca^{2+}]$_i$ concentration. The pH$_i$ sensitivity values were slopes from linear fit shown in D under different Ca^{2+} concentrations. The smooth line was fitted with a bell-shaped dose–response curve using GraphPad Prism, with peak pH sensitivity of 0.33 at ~15 µM Ca^{2+}. The error bars represent SEM (n = 5).

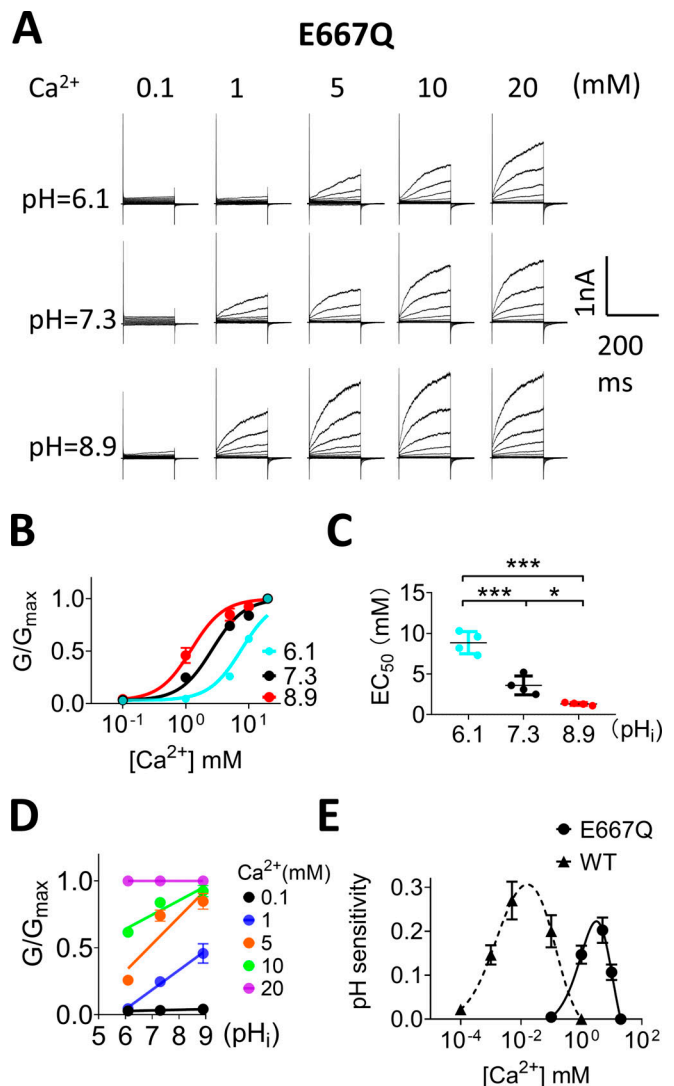Figure 6. **Ca^{2+} binding sites mediate pH$_i$ regulation on TMEM16F. (A)** Representative TMEM16F-E667Q currents recorded from inside-out patches perfused with intracellular solutions containing 0.1, 1, 5, 10, and 20 mM Ca^{2+} at different pH$_i$ values. **(B)** Ca^{2+} dose–response of TMEM16F-E667Q mutation. The error bars represent SEM (n = 4). **(C)** EC$_{50}$ values of Ca^{2+} at pH$_i$ 6.1, 7.3, and 8.9 were 8.64 ± 1.08, 2.93 ± 0.42, and 1.22 ± 0.31 mM, respectively. The error bars represent SEM (n = 4). P values were determined with Tukey test comparisons after one-way ANOVA: ***, P < 0.001; *, P < 0.5. **(D)** The G-pH$_i$ relationship of TMEM16F-E667Q. Solid lines represent linear fits. **(E)** The pH$_i$ sensitivity and [Ca^{2+}]$_i$ concentration relationship of E667Q (solid line). The peak pH sensitivity is 0.22 at ~3.01 mM Ca^{2+}. The error bars represent SEM (n = 4). Curve from WT (dashed line) was replotted here for reference.

neutralized its acidic residues D859A and E395A and examined their pH$_i$ regulation (Fig. S7). We found that both mutations showed no effect on pH$_i$ sensitivity, as evidenced by indistinguishable G-pH$_i$ relationships between the mutant and WT channels (Fig. S7 E). We concluded that the primary Ca^{2+} binding sites in the pore but not the third Ca^{2+} binding site near the dimer interface are responsible for TMEM16F pH$_i$ regulation.

Taken together, our systematic biophysical characterizations and mutagenesis experiments explicitly illustrate a pH$_i$ regulatory mechanism for both TMEM16F and TMEM16A. According to this mechanism, pH$_i$ regulates the activation of these TMEM16 proteins through protonation and deprotonation of their primary Ca^{2+} binding sites, which in turn reduce and enhance their Ca^{2+} binding affinity, respectively (Fig. 7). As the Ca^{2+} binding residues are highly conserved, this pH$_i$ regulatory mechanism may also apply to other TMEM16 family members.
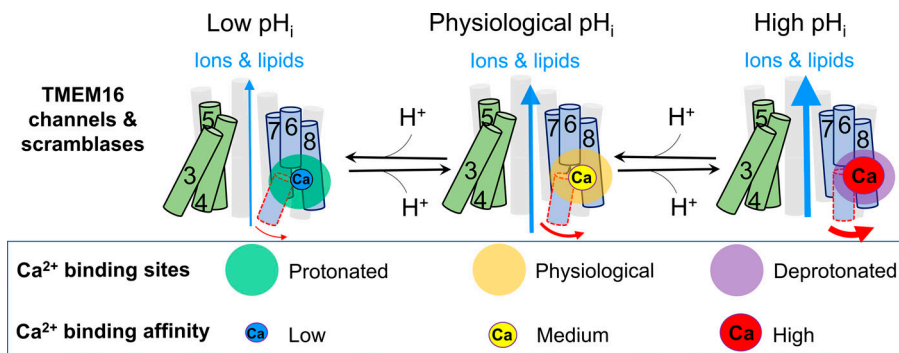
Figure 7. **Schematic model of pH$_i$ regulation on TMEM16F and TMEM16A under physiological Ca^{2+}$_i$.** Under low pH$_i$ conditions, protonation of the primary Ca^{2+} binding residues in the pore can significantly reduce Ca^{2+} binding affinity of TMEM16 proteins and suppress their activation. In contrast, high pH$_i$ deprotonates the Ca^{2+} binding residues and enhances Ca^{2+} binding and TMEM16 activation. The size of blue arrows represents the open probability of TMEM16 proteins. The size of Ca^{2+} ions represents the strength of apparent Ca^{2+} binding affinity.

Discussion

In this study, we systematically investigated the pH$_i$ effects on TMEM16F CaPLSase and ion channel activities using the lipid scrambling–fluorometry assay and inside-out patch clamp recording, respectively. We discovered that pH$_i$ can effectively regulate TMEM16F CaPLSase and ion channel activities. By comparing with the pH$_i$ regulation of TMEM16A-CaCC, we conclude that pH$_i$ regulates TMEM16F and TMEM16A activation through the same molecular mechanism. Our biophysical characterizations and mutagenesis studies explicitly show that the primary Ca^{2+} binding residues within the pore of the TMEM16 proteins serve as the pH$_i$ sensors (Fig. 7). Protonation of the carboxylate groups of the Ca^{2+} binding residues prevents Ca^{2+} binding, thereby hindering TMEM16 activation. In contrast, deprotonation of the carboxylate groups of the Ca^{2+} binding residues facilitates Ca^{2+} binding, thereby promoting TMEM16 activation.

Histidine, the most titratable amino acid under physiological pH$_i$ range, is unlikely to be the pH$_i$ sensor for TMEM16F activation. The previous mutagenesis study of TMEM16A demonstrates that all the intracellular histidine-to-alanine mutations do not alter the inhibitory effect of proton on TMEM16A activation (Chun et al., 2015). As some of these histidine residues are conserved between TMEM16F and TMEM16A, it is thus plausible to assert that the equivalent histidine residues also do not contribute to TMEM16F pH$_i$ sensing. In addition, our characterizations of the gain-of-function mutations of TMEM16F and TMEM16A channels showed that these gain-of-function mutant channels are insensitive to pH$_i$ regulation (Fig. S6). If some of the intracellular histidine residues contribute to pH$_i$ sensing, the pH$_i$ sensitivity of the gain-of-function mutant channels should be altered. Therefore, the intracellular histidine residues are unlikely to contribute to pH$_i$ regulation.

pH$_i$ regulation of TMEM16F ion channel activity can be precisely measured using inside-out patch clamping. Nevertheless, accurate quantification of the pH$_i$ effects on TMEM16F CaPLSase activity has been challenging. First, the fluorescent assays to detect CaPLSase activities are less sensitive than patch clamping. Fluorescently tagged AnV has been commonly used as a PS probe, whose time-dependent accumulation on cell surface serves as a readout of CaPLSase activities. Unlike patch clamping that can detect the activities of a small number of channels or even single-channel activities, reliable measurement of CaPLSase activities requires an ensemble of CaPLSases, usually in a

large population of cells or, under higher-resolution microscopy, the entire single cells. Second, compared with patch-clamp recording of ion channel activities, CaPLSase-mediated AnV binding is slow (takes tens of minutes to reach steady-state) and hardly reversible. Third, it is challenging to precisely control intracellular Ca^{2+}, which is required to accurately measure CaPLSase activities. The patch clamp-lipid scrambling fluorometry assay developed by the Hartzell laboratory uses the patch pipette to infuse defined Ca^{2+} into a patched cell (Yu et al., 2015), thereby enabling precise control of intracellular Ca^{2+} and measurement of CaPLSase activities at the single-cell level. Nevertheless, quantitative analysis of the CaPLSase activities has not been established, which hinders the application of the patch-clamping lipid scrambling–fluorometry assay to study TMEM16 CaPLSase activation and regulation.

In this study, we modified the patch-clamping lipid scrambling–fluorometry assay to achieve precise control of both [Ca^{2+}]$_i$ and pH$_i$ (Fig. 2 A). By measuring and fitting the time-dependent increase of AnV fluorescence with a generalized logistic equation, we can obtain three parameters, t_{on}, $t_{1/2}$, and slope k. t_{on} is the onset time of macroscopic CaPLSase activity. It represents the lag time needed for Ca^{2+} to diffuse from the pipette solution to cytosol and reach the threshold Ca^{2+} concentration to trigger sufficient CaPLSase activities that can be reliably detected by our fluorescence microscope. The t_{on} for TMEM16F CaPLSase is ~11 min under 100 µM Ca^{2+} and pH$_i$ 7.3, which is comparable to the previous reported lag time of TMEM16F CaPLSase (Yu et al., 2015) and TMEM16F channel under whole-cell configuration (Grubb et al., 2013; Yu et al., 2015). Paradoxically, TMEM16F current can be instantaneously activated without delay under inside-out configuration (Fig. 1 A; Fig. 3, A and B; and Fig. 5 A). It is still unclear why TMEM16F activation needs such a long t_{on} compared with the fast activation of TMEM16A-CaCC activation under whole-cell configuration. The lower Ca^{2+} sensitivity of TMEM16F (Yang et al., 2012; Yu et al., 2015) and also the potential interaction between TMEM16F and cytoskeleton could contribute to this long lag time (Lin et al., 2018; Roh and Nam, 2020). Future studies are needed to further dissect out the underlying mechanism of the long lag time for TMEM16F activation. Nevertheless, t_{on} for TMEM16F activation is apparently Ca^{2+} dependent, as shown in Fig. 2 D and Fig. 4, C and H. The higher the Ca^{2+}, the shorter the t_{on} under any given pH$_i$. We also obtained $t_{1/2}$ for TMEM16F CaPLSases, which is the time needed to reach half-maximum

AnV fluorescence after membrane break-in, as an additional parameter to evaluate CaPLSase activity. $t_{1/2}$ is the summation of t_{on} and the time needed from t_{on} to reach half-maximum AnV fluorescence. $t_{1/2}$ is thus determined by two factors: t_{on} and the scrambling rate of the active TMEM16F CaPLSase for PS permeation. The macroscopic TMEM16F scrambling rate gradually increases over time after t_{on}, reflecting the augments of TMEM16F open probability and conductance for phospholipids. Different from ion transport that usually operates with constant ion gradients, phospholipid flip-flop across the membrane bilayer is controlled by finite phospholipid gradients, which gradually dissipate with prolonged scramblase activation. Thus, CaPLSase phospholipid scrambling reaches maximum rate at $t_{1/2}$ and then gradually decreases until phospholipids become symmetrically distributed. The maximum apparent CaPLSase scrambling rate is measured as the slope k of the linear phase of the sigmoid curve at $t_{1/2}$. This is the third parameter to evaluate CaPLSase activity.

Remarkably, pH$_i$ exerts similar impacts on t_{on}, $t_{1/2}$, and slope k of the TMEM16F CaPLSases regardless of the biophysical meanings of the parameters (Fig. 2, C–F; and Fig. 4, B–E and G–J). Under nonsaturating Ca^{2+} (5 and 100 µM), low pH$_i$ prolongs both t_{on} and $t_{1/2}$ and reduces slope k, whereas high pH$_i$ shortens both t_{on} and $t_{1/2}$ and increases slope k. The comparison of these parameters thus suggests that pH$_i$ strongly controls TMEM16F CaPLSase Ca^{2+}-dependent activation and phospholipid permeation. We hope that our detailed biophysical characterization and quantification of CaPLSase activity and our interpretation of the underlying biophysical meanings of the parameters can inspire the field to further dissect the molecular mechanisms of TMEM16 CaPLSases and facilitate future biophysical, physiological, and pharmacological characterizations of these intriguing membrane transporters.

Interestingly, pH$_i$ sensitivity of TMEM16F is highly Ca^{2+} dependent and exhibits a bell-shaped relationship with [Ca^{2+}]$_i$ (Fig. 5 E). According to this relationship, saturating [Ca^{2+}]$_i$ can override the pH$_i$ effects on the protonation states of the Ca^{2+} binding residues, thereby eliminating pH$_i$ sensitivity for WT TMEM16F and TMEM16A (Fig. 3, D and E; Fig. 4, G–J; and Fig. S5). Mutating the Ca^{2+} binding residues dramatically reduces TMEM16F apparent Ca^{2+} sensitivity (Fig. 6, B and C; Yang et al., 2012; Yu et al., 2012; Tien et al., 2014; Alvadia et al., 2019), which results in a significant right shift of the bell shape of the pH$_i$-Ca^{2+} curve (Fig. 6 E). The notable reduction of the peak pH$_i$ sensitivity as well as the narrowed pH$_i$-Ca^{2+} curve suggest that the overall pH$_i$ effect diminishes in the Ca^{2+} binding site mutation of TMEM16F. On the other hand, we also show evidence that pH$_i$ exerts a negligible effect on the pore-lining residue Q559K (Fig. S3) and the Ca^{2+} binding site located in the dimer interface of TMEM16F (Fig. S7), suggesting that the two primary Ca^{2+} binding sites predominantly mediate the pH$_i$ regulatory effects on TMEM16 protein. In addition, when [Ca^{2+}]$_i$ is very low and voltage plays a more prominent role in activating the TMEM16 proteins, the pH$_i$ sensitivities of TMEM16F and TMEM16A reduce. This is likely because pH$_i$ has negligible impact on voltage-dependent activation of these proteins, as evidenced by the near-parallel G-pH_i relationships across a wide range of

activation voltages (Figs. 1 C and S1 C), as well as the lack of pH$_i$ effects on the voltage-dependent activation of the gain-of-function mutations of TMEM16F and TMEM16F in the absence of [Ca^{2+}]$_i$ (Fig. S6). It is worth noting that all our experiments were conducted at room temperature. According to a recent publication (Lin et al., 2019), TMEM16F is more sensitive to [Ca^{2+}]$_i$ at 37°C. It is therefore plausible that pH$_i$ may be more sensitive to [Ca^{2+}]$_i$ at physiological temperature.

Intracellular alkalization is one of the hallmarks of cancer cells (Webb et al., 2011). A number of distinct ion transporters and pumps, including the Na$^+$-H$^+$ exchangers (Lauritzen et al., 2012), the H$^+$/K$^+$-ATPase proton pump (Goh et al., 2014), and the Na$^+$-driven bicarbonate transporters (McIntyre et al., 2016), have been known to contribute to intracellular alkalization. Unlike the extensive understanding of pH$_i$ dysregulation in cancer cells, how intracellular alkalization affects cancer cell function is still elusive. Interestingly, TMEM16F has been identified in a wide variety of cancer cells, and according to the Human Protein Atlas (http://www.proteinatlas.org), the high expression level of TMEM16F is associated with the overall prognosis of a number of cancers including breast and cervical cancer. Although it is unclear how TMEM16F contributes to tumor growth and cancer progression, it has been reported that genetic manipulations of TMEM16F can change cancer cell proliferation and migration (Jacobsen et al., 2013; Wang et al., 2018; Xuan et al., 2019). Interestingly, loss of membrane phospholipid asymmetry is a salient feature of many cancerous cells, whose cell surfaces display an elevated amount of PS (Riedl et al., 2011; Zhao et al., 2011). It is still unclear which phospholipid transporters are responsible for the enhanced PS exposure on the surfaces of the cancer cells. Nevertheless, no sign of apoptosis (Utsugi et al., 1991) and the beneficial effects of PS exposure to cancer cell survival (Schröder-Borm et al., 2005; He et al., 2009; Kenis and Reutelingsperger, 2009; Gerber et al., 2011; Blanco et al., 2014; Zhang et al., 2014) suggest that CaPLSases instead of caspase-dependent lipid scramblases may play important roles in facilitating PS exposure in cancer cells. Our current investigation of the mechanism of TMEM16F pH$_i$ regulation thus lays a foundation to further understand the role of TMEM16F in cancer and other physiological or pathological conditions, in which pH$_i$ fluctuates or is dysregulated. The shared molecular mechanism of pH$_i$ regulation between TMEM16F and TMEM16A identified in this study will also facilitate our understanding of the regulatory mechanism and physiological functions of other TMEM16 family members.

Acknowledgments

References

Alvadia, C., N.K. Lim, V. Clerico Mosina, G.T. Oostergetel, R. Dutzler, and C. Paulino. 2019. Cryo-EM structures and functional characterization of the murine lipid scramblase TMEM16F. *eLife.* 8:e44365. https://doi.org/10.7554/eLife.44365

Arreola, J., J.E. Melvin, and T. Begenisich. 1995. Inhibition of Ca(2+)-dependent Cl⁻ channels from secretory epithelial cells by low internal pH. *J. Membr. Biol.* 147:95–104. https://doi.org/10.1007/BF00235400

Berg, J., H. Yang, and L.Y. Jan. 2012. Ca2+-activated Cl⁻ channels at a glance. *J. Cell Sci.* 125:1367–1371. https://doi.org/10.1242/jcs.093260

Bezprozvanny, I., J. Watras, and B.E. Ehrlich. 1991. Bell-shaped calcium-response curves of Ins(1,4,5)P3- and calcium-gated channels from endoplasmic reticulum of cerebellum. *Nature.* 351:751–754. https://doi.org/10.1038/351751a0

Blanco, V.M., Z. Chu, S.D. Vallabhapurapu, M.K. Sulaiman, A. Kendler, O. Rixe, R.E. Warnick, R.S. Franco, and X. Qi. 2014. Phosphatidylserine-selective targeting and anticancer effects of SapC-DOPS nanovesicles on brain tumors. *Oncotarget.* 5:7105–7118. https://doi.org/10.18632/oncotarget.2214

Brunner, J.D., N.K. Lim, S. Schenck, A. Duerst, and R. Dutzler. 2014. X-ray structure of a calcium-activated TMEM16 lipid scramblase. *Nature.* 516:207–212. https://doi.org/10.1038/nature13984

Brunner, J.D., S. Schenck, and R. Dutzler. 2016. Structural basis for phospholipid scrambling in the TMEM16 family. Curr. Opin. Struct. Biol. 39:61–70.

Bushell, S.R., A.C.W. Pike, M.E. Falzone, N.J.G. Rorsman, C.M. Ta, R.A. Corey, T.D. Newport, J.C. Christianson, L.F. Scofano, C.A. Shintre, et al. 2019. The structural basis of lipid scrambling and inactivation in the endoplasmic reticulum scramblase TMEM16K. *Nat. Commun.* 10:3956. https://doi.org/10.1038/s41467-019-11753-1

Caputo, A., E. Caci, L. Ferrera, N. Pedemonte, C. Barsanti, E. Sondo, U. Pfeffer, R. Ravazzolo, O. Zegarra-Moran, and L.J.V. Galietta. 2008. TMEM16A, a membrane protein associated with calcium-dependent chloride channel activity. *Science.* 322:590–594. https://doi.org/10.1126/science.1163518

Castoldi, E., P.W. Collins, P.L. Williamson, and E.M. Bevers. 2011. Compound heterozygosity for 2 novel TMEM16F mutations in a patient with Scott syndrome. *Blood.* 117:4399–4400. https://doi.org/10.1182/blood-2011-01-332502

Cho, H., Y.D. Yang, J. Lee, B. Lee, T. Kim, Y. Jang, S.K. Back, H.S. Na, B.D. Harfe, F. Wang, et al. 2012. The calcium-activated chloride channel anoctamin 1 acts as a heat sensor in nociceptive neurons. *Nat. Neurosci.* 15:1015–1021. https://doi.org/10.1038/nn.3111

Chun, H., H. Cho, J. Choi, J. Lee, S.M. Kim, H. Kim, and U. Oh. 2015. Protons inhibit anoctamin 1 by competing with calcium. *Cell Calcium.* 58:431–441. https://doi.org/10.1016/j.ceca.2015.06.011

Crottès, D., and L.Y. Jan. 2019. The multifaceted role of TMEM16A in cancer. *Cell Calcium.* 82:102050. https://doi.org/10.1016/j.ceca.2019.06.004

Cruz-Rangel, S., J.J. De Jesús-Pérez, I.A. Aréchiga-Figueroa, A.A. Rodríguez-Menchaca, P. Pérez-Cornejo, H.C. Hartzell, and J. Arreola. 2017. Extracellular protons enable activation of the calcium-dependent chloride channel TMEM16A. *J. Physiol.* 595:1515–1531. https://doi.org/10.1113/JP273111

Dang, S., S. Feng, J. Tien, C.J. Peters, D. Bulkley, M. Lolicato, J. Zhao, K. Zuberbühler, W. Ye, L. Qi, et al. 2017. Cryo-EM structures of the TMEM16A calcium-activated chloride channel. *Nature.* 552:426–429. https://doi.org/10.1038/nature25024

De Jesús-Pérez, J.J., S. Cruz-Rangel, Á.E. Espino-Saldaña, A. Martínez-Torres, Z. Qu, H.C. Hartzell, N.E. Corral-Fernandez, P. Pérez-Cornejo, and J. Arreola. 2018. Phosphatidylinositol 4,5-bisphosphate, cholesterol, and fatty acids modulate the calcium-activated chloride channel TMEM16A (ANO1). *Biochim. Biophys. Acta Mol. Cell Biol. Lipids.* 1863:299–312. https://doi.org/10.1016/j.bbalip.2017.12.009

Ehlen, H.W.A., M. Chinenkova, M. Moser, H.-M. Munter, Y. Krause, S. Gross, B. Brachvogel, M. Wuelling, U. Kornak, and A. Vortkamp. 2013. Inactivation of anoctamin-6/Tmem16f, a regulator of phosphatidylserine scrambling in osteoblasts, leads to decreased mineral deposition in skeletal tissues. *J. Bone Miner. Res.* 28:246–259. https://doi.org/10.1002/jbmr.1751

Falzone, M.E., M. Malvezzi, B.-C. Lee, and A. Accardi. 2018. Known structures and unknown mechanisms of TMEM16 scramblases and channels. *J. Gen. Physiol.* 150:933–947. https://doi.org/10.1085/jgp.201711957

Feng, S., S. Dang, T.W. Han, W. Ye, P. Jin, T. Cheng, J. Li, Y.N. Jan, L.Y. Jan, and Y. Cheng. 2019. Cryo-EM Studies of TMEM16F Calcium-Activated Ion Channel Suggest Features Important for Lipid Scrambling. *Cell Rep.* 28:567–579.e4. https://doi.org/10.1016/j.celrep.2019.06.023

Fujii, T., A. Sakata, S. Nishimura, K. Eto, and S. Nagata. 2015. TMEM16F is required for phosphatidylserine exposure and microparticle release in activated mouse platelets. *Proc. Natl. Acad. Sci. USA.* 112:12800–12805. https://doi.org/10.1073/pnas.1516594112

Gerber, D.E., A.T. Stopeck, L. Wong, L.S. Rosen, P.E. Thorpe, J.S. Shan, and N.K. Ibrahim. 2011. Phase I safety and pharmacokinetic study of bavituximab, a chimeric phosphatidylserine-targeting monoclonal antibody, in patients with advanced solid tumors. *Clin. Cancer Res.* 17:6888–6896. https://doi.org/10.1158/1078-0432.CCR-11-1074

Goh, W., I. Sleptsova-Freidrich, and N. Petrovic. 2014. Use of proton pump inhibitors as adjunct treatment for triple-negative breast cancers. An introductory study. *J. Pharm. Pharm. Sci.* 17:439–446. https://doi.org/10.18433/J34608

Grubb, S., K.A. Poulsen, C.A. Juul, T. Kyed, T.K. Klausen, E.H. Larsen, and E.K. Hoffmann. 2013. TMEM16F (Anoctamin 6), an anion channel of delayed Ca^{2+} activation. *J. Gen. Physiol.* 141:585–600. https://doi.org/10.1085/jgp.201210861

Hartzell, C., I. Putzier, and J. Arreola. 2005. Calcium-activated chloride channels. *Annu. Rev. Physiol.* 67:719–758. https://doi.org/10.1146/annurev.physiol.67.032003.154341

He, J., Y. Yin, T.A. Luster, L. Watkins, and P.E. Thorpe. 2009. Anti-phosphatidylserine antibody combined with irradiation damages tumor blood vessels and induces tumor immunity in a rat model of glioblastoma. *Clin. Cancer Res.* 15:6871–6880. https://doi.org/10.1158/1078-0432.CCR-09-1499

Huang, F., X. Wang, E.M. Ostertag, T. Nuwal, B. Huang, Y.-N. Jan, A.I. Basbaum, and L.Y. Jan. 2013. TMEM16C facilitates Na(+)-activated K+ currents in rat sensory neurons and regulates pain processing. *Nat. Neurosci.* 16:1284–1290. https://doi.org/10.1038/nn.3468

Huang, W.C., S. Xiao, F. Huang, B.D. Harfe, Y.N. Jan, and L.Y. Jan. 2012. Calcium-activated chloride channels (CaCCs) regulate action potential and synaptic response in hippocampal neurons. *Neuron.* 74:179–192. https://doi.org/10.1016/j.neuron.2012.01.033

Jacobsen, K.S., K. Zeeberg, D.R.P. Sauter, K.A. Poulsen, E.K. Hoffmann, and A. Schwab. 2013. The role of TMEM16A (ANO1) and TMEM16F (ANO6) in cell migration. *Pflugers Arch.* 465:1753–1762. https://doi.org/10.1007/s00424-013-1315-z

Kenis, H., and C. Reutelingsperger. 2009. Targeting phosphatidylserine in anti-cancer therapy. *Curr. Pharm. Des.* 15:2719–2723. https://doi.org/10.2174/138161209788923903

Lagadic-Gossmann, D., L. Huc, and V. Lecureur. 2004. Alterations of intracellular pH homeostasis in apoptosis: origins and roles. *Cell Death Differ.* 11:953–961. https://doi.org/10.1038/sj.cdd.4401466

Lauritzen, G., C.-M. Stock, J. Lemaire, S.F. Lund, M.F. Jensen, B. Damsgaard, K.S. Petersen, L. Wiwel, L. Rønnov-Jessen, A. Schwab, and S.F. Pedersen. 2012. The Na+/H+ exchanger NHE1, but not the Na+, HCO3(-) cotransporter NBCn1, regulates motility of MCF7 breast cancer cells expressing constitutively active ErbB2. *Cancer Lett.* 317:172–183. https://doi.org/10.1016/j.canlet.2011.11.023

Le, S.C., Z. Jia, J. Chen, and H. Yang. 2019a. Molecular basis of PIP$_2$-dependent regulation of the Ca^{2+}-activated chloride channel TMEM16A. *Nat. Commun.* 10:3769. https://doi.org/10.1038/s41467-019-11784-8

Le, T., Z. Jia, S.C. Le, Y. Zhang, J. Chen, and H. Yang. 2019b. An inner activation gate controls TMEM16F phospholipid scrambling. *Nat. Commun.* 10:1846. https://doi.org/10.1038/s41467-019-09778-7

Le, T., S.C. Le, and H. Yang. 2019c. *Drosophila* Subdued is a moonlighting transmembrane protein 16 (TMEM16) that transports ions and phospholipids. *J. Biol. Chem.* 294:4529–4537. https://doi.org/10.1074/jbc.AC118.006530

Li, K.X., M. He, W. Ye, J. Simms, M. Gill, X. Xiang, Y.N. Jan, and L.Y. Jan. 2019. TMEM16B regulates anxiety-related behavior and GABAergic neuronal signaling in the central lateral amygdala. *eLife.* 8:e47106. https://doi.org/10.7554/eLife.47106

Lin, H., I. Jun, J.H. Woo, M.G. Lee, S.J. Kim, and J.H. Nam. 2019. Temperature-dependent increase in the calcium sensitivity and acceleration of activation of ANO6 chloride channel variants. *Sci. Rep.* 9:6706. https://doi.org/10.1038/s41598-019-43162-1

Lin, H., J. Roh, J.H. Woo, S.J. Kim, and J.H. Nam. 2018. TMEM16F/ANO6, a Ca^{2+}-activated anion channel, is negatively regulated by the actin cytoskeleton and intracellular MgATP. *Biochem. Biophys. Res. Commun.* 503:2348–2354. https://doi.org/10.1016/j.bbrc.2018.06.160

McIntyre, A., A. Hulikova, I. Ledaki, C. Snell, D. Singleton, P. Seden, D. Jones, E. Bridges, S. Wigfield, et al. 2016. Disrupting hypoxia-induced bicarbonate transport acidifies tumor cells and suppresses tumor growth. *Cancer Res.* 76:3744–3755. https://doi.org/10.1158/0008-5472.CAN-15-1862

Oh, U., and J. Jung. 2016. Cellular functions of TMEM16/anoctamin. *Pflugers Arch.* 468:443–453. https://doi.org/10.1007/s00424-016-1790-0

Ousingsawat, J., P. Wanitchakool, R. Schreiber, M. Wuelling, A. Vortkamp, and K. Kunzelmann. 2015. Anoctamin-6 controls bone mineralization by activating the calcium transporter NCX1. *J. Biol. Chem.* 290:6270–6280. https://doi.org/10.1074/jbc.M114.602979

Park, K., and P.D. Brown. 1995. Intracellular pH modulates the activity of chloride channels in isolated lacrimal gland acinar cells. *Am. J. Physiol.* 268:C647–C650. https://doi.org/10.1152/ajpcell.1995.268.3.C647

Paulino, C., V. Kalienkova, A.K.M. Lam, Y. Neldner, and R. Dutzler. 2017. Activation mechanism of the calcium-activated chloride channel TMEM16A revealed by cryo-EM. *Nature.* 552:421–425. https://doi.org/10.1038/nature24652

Pedemonte, N., and L.J.V. Galietta. 2014. Structure and function of TMEM16 proteins (anoctamins). *Physiol. Rev.* 94:419–459. https://doi.org/10.1152/physrev.00039.2011

Peters, C.J., J.M. Gilchrist, J. Tien, N.P. Bethel, L. Qi, T. Chen, L. Wang, Y.N. Jan, M. Grabe, and L.Y. Jan. 2018. The Sixth Transmembrane Segment Is a Major Gating Component of the TMEM16A Calcium-Activated Chloride Channel. *Neuron.* 97:1063–1077.e4. https://doi.org/10.1016/j.neuron.2018.01.048

Qu, Z., and H.C. Hartzell. 2000. Anion permeation in $Ca^{(2+)}$-activated $Cl^{(-)}$ channels. *J. Gen. Physiol.* 116:825–844. https://doi.org/10.1085/jgp.116.6.825

Riedl, S., B. Rinner, M. Asslaber, H. Schaider, S. Walzer, A. Novak, K. Lohner, and D. Zweytick. 2011. In search of a novel target - phosphatidylserine exposed by non-apoptotic tumor cells and metastases of malignancies with poor treatment efficacy. *Biochim. Biophys. Acta.* 1808:2638–2645. https://doi.org/10.1016/j.bbamem.2011.07.026

Roh, J.W., and J.H. Nam. 2020. Various Physiological Factors for Regulating Activation Speeds in the Delayed Calcium-Dependent Activation of ANO6/TMEM16F. *FASEB J.* 34(S1):1. https://doi.org/10.1096/fasebj.2020.34.s1.03231

Schröder-Borm, H., R. Bakalova, and J. Andrä. 2005. The NK-lysin derived peptide NK-2 preferentially kills cancer cells with increased surface levels of negatively charged phosphatidylserine. *FEBS Lett.* 579:6128–6134. https://doi.org/10.1016/j.febslet.2005.09.084

Schroeder, B.C., T. Cheng, Y.N. Jan, and L.Y. Jan. 2008. Expression cloning of TMEM16A as a calcium-activated chloride channel subunit. *Cell.* 134:1019–1029. https://doi.org/10.1016/j.cell.2008.09.003

Segura-Covarrubias, G., I.A. Aréchiga-Figueroa, J.J. De Jesús-Pérez, A. Sánchez-Solano, P. Pérez-Cornejo, and J. Arreola. 2020. Voltage-Dependent Protonation of the Calcium Pocket Enable Activation of the Calcium-Activated Chloride Channel Anoctamin-1 (TMEM16A). *Sci. Rep.* 10:6644. https://doi.org/10.1038/s41598-020-62860-9

Suzuki, J., E. Imanishi, and S. Nagata. 2014. Exposure of phosphatidylserine by Xk-related protein family members during apoptosis. *J. Biol. Chem.* 289:30257–30267. https://doi.org/10.1074/jbc.M114.583419

Suzuki, J., M. Umeda, P.J. Sims, and S. Nagata. 2010. Calcium-dependent phospholipid scrambling by TMEM16F. *Nature.* 468:834–838. https://doi.org/10.1038/nature09583

Ta, C.M., K.E. Acheson, N.J.G. Rorsman, R.C. Jongkind, and P. Tammaro. 2017. Contrasting effects of phosphatidylinositol 4,5-bisphosphate on cloned TMEM16A and TMEM16B channels. *Br. J. Pharmacol.* 174:2984–2999. https://doi.org/10.1111/bph.13913

Tembo, M., K.L. Wozniak, R.E. Bainbridge, and A.E. Carlson. 2019. Phosphatidylinositol 4,5-bisphosphate (PIP_2) and Ca^{2+} are both required to open the Cl^- channel TMEM16A. *J. Biol. Chem.* 294:12556–12564. https://doi.org/10.1074/jbc.RA118.007128

Tien, J., C.J. Peters, X.M. Wong, T. Cheng, Y.N. Jan, L.Y. Jan, and H. Yang. 2014. A comprehensive search for calcium binding sites critical for TMEM16A calcium-activated chloride channel activity. *eLife.* 3:e02772. https://doi.org/10.7554/eLife.02772

Utsugi, T., A.J. Schroit, J. Connor, C.D. Bucana, and I.J. Fidler. 1991. Elevated expression of phosphatidylserine in the outer membrane leaflet of human tumor cells and recognition by activated human blood monocytes. *Cancer Res.* 51:3062–3066.

Wang, L., X.-Y. Zhao, J.-S. Zhu, N.-W. Chen, H.-N. Fan, W. Yang, and J.-H. Guo. 2018. CCR7 regulates ANO6 to promote migration of pancreatic ductal adenocarcinoma cells via the ERK signaling pathway. *Oncol. Lett.* 16:2599–2605. https://doi.org/10.3892/ol.2018.8962

Webb, B.A., M. Chimenti, M.P. Jacobson, and D.L. Barber. 2011. Dysregulated pH: a perfect storm for cancer progression. *Nat. Rev. Cancer.* 11:671–677. https://doi.org/10.1038/nrc3110

White, K.A., B.K. Grillo-Hill, and D.L. Barber. 2017. Cancer cell behaviors mediated by dysregulated pH dynamics at a glance. *J. Cell Sci.* 130:663–669. https://doi.org/10.1242/jcs.195297

Whitlock, J.M., and H.C. Hartzell. 2017. Anoctamins/TMEM16 Proteins: Chloride Channels Flirting with Lipids and Extracellular Vesicles. *Annu. Rev. Physiol.* 79:119–143. https://doi.org/10.1146/annurev-physiol-022516-034031

Whitlock, J.M., K. Yu, Y.Y. Cui, and H.C. Hartzell. 2018. Anoctamin 5/TMEM16E facilitates muscle precursor cell fusion. *J. Gen. Physiol.* 150:1498–1509. https://doi.org/10.1085/jgp.201812097

Xuan, Z.B., Y.J. Wang, and J. Xie. 2019. ANO6 promotes cell proliferation and invasion in glioma through regulating the ERK signaling pathway. *OncoTargets Ther.* 12:6721–6731. https://doi.org/10.2147/OTT.S211725

Yang, H., A. Kim, T. David, D. Palmer, T. Jin, J. Tien, F. Huang, T. Cheng, S.R. Coughlin, Y.N. Jan, and L.Y. Jan. 2012. TMEM16F forms a Ca2+-activated cation channel required for lipid scrambling in platelets during blood coagulation. *Cell.* 151:111–122. https://doi.org/10.1016/j.cell.2012.07.036

Yang, Y.D., H. Cho, J.Y. Koo, M.H. Tak, Y. Cho, W.-S. Shim, S.P. Park, J. Lee, B. Lee, B.-M. Kim, et al. 2008. TMEM16A confers receptor-activated calcium-dependent chloride conductance. *Nature.* 455:1210–1215. https://doi.org/10.1038/nature07313

Ye, W., T.W. Han, L.M. Nassar, M. Zubia, Y.N. Jan, and L.Y. Jan. 2018. Phosphatidylinositol-(4, 5)-bisphosphate regulates calcium gating of small-conductance cation channel TMEM16F. *Proc. Natl. Acad. Sci. USA.* 115:E1667–E1674. https://doi.org/10.1073/pnas.1718728115

Yin, X., J. Goudriaan, E.A. Lantinga, J. Vos, and H.J. Spiertz. 2003. A flexible sigmoid function of determinate growth. *Ann. Bot.* 91:361–371. https://doi.org/10.1093/aob/mcg029

Yu, K., C. Duran, Z. Qu, Y.-Y. Cui, and H.C. Hartzell. 2012. Explaining calcium-dependent gating of anoctamin-1 chloride channels requires a revised topology. *Circ. Res.* 110:990–999. https://doi.org/10.1161/CIRCRESAHA.112.264440

Yu, K., T. Jiang, Y. Cui, E. Tajkhorshid, and H.C. Hartzell. 2019. A network of phosphatidylinositol 4,5-bisphosphate binding sites regulates gating of the Ca^{2+}-activated Cl^- channel ANO1 (TMEM16A). *Proc. Natl. Acad. Sci. USA.* 116:19952–19962. https://doi.org/10.1073/pnas.1904012116

Yu, K., J.M. Whitlock, K. Lee, E.A. Ortlund, Y.Y. Cui, and H.C. Hartzell. 2015. Identification of a lipid scrambling domain in ANO6/TMEM16F. *eLife.* 4:e06901. https://doi.org/10.7554/eLife.06901

Zaitseva, E., E. Zaitsev, K. Melikov, A. Arakelyan, M. Marin, R. Villasmil, L.B. Margolis, G.B. Melikyan, and L.V. Chernomordik. 2017. Fusion Stage of HIV-1 Entry Depends on Virus-Induced Cell Surface Exposure of Phosphatidylserine. *Cell Host Microbe.* 22:99–110.e7. https://doi.org/10.1016/j.chom.2017.06.012

Zhang, L., H. Zhou, O. Belzile, P. Thorpe, and D. Zhao. 2014. Phosphatidylserine-targeted bimodal liposomal nanoparticles for in vivo imaging of breast cancer in mice. *J. Control. Release.* 183:114–123. https://doi.org/10.1016/j.jconrel.2014.03.043

Zhang, Y., T. Le, R. Grabau, Z. Mohseni, H. Kim, D.R. Natale, L. Feng, H. Pan, and H. Yang. 2020. TMEM16F phospholipid scramblase mediates trophoblast fusion and placental development. *Sci. Adv.* 6:eaba0310. https://doi.org/10.1126/sciadv.aba0310

Zhang, Y., Z. Zhang, S. Xiao, J. Tien, S. Le, T. Le, L.Y. Jan, and H. Yang. 2017. Inferior Olivary TMEM16B Mediates Cerebellar Motor Learning. *Neuron.* 95:1103–1111.e4. https://doi.org/10.1016/j.neuron.2017.08.010

Zhao, D., J.H. Stafford, H. Zhou, and P.E. Thorpe. 2011. Near-infrared Optical Imaging of Exposed Phosphatidylserine in a Mouse Glioma Model. *Transl. Oncol.* 4:355–364. https://doi.org/10.1593/tlo.11178

Supplemental material
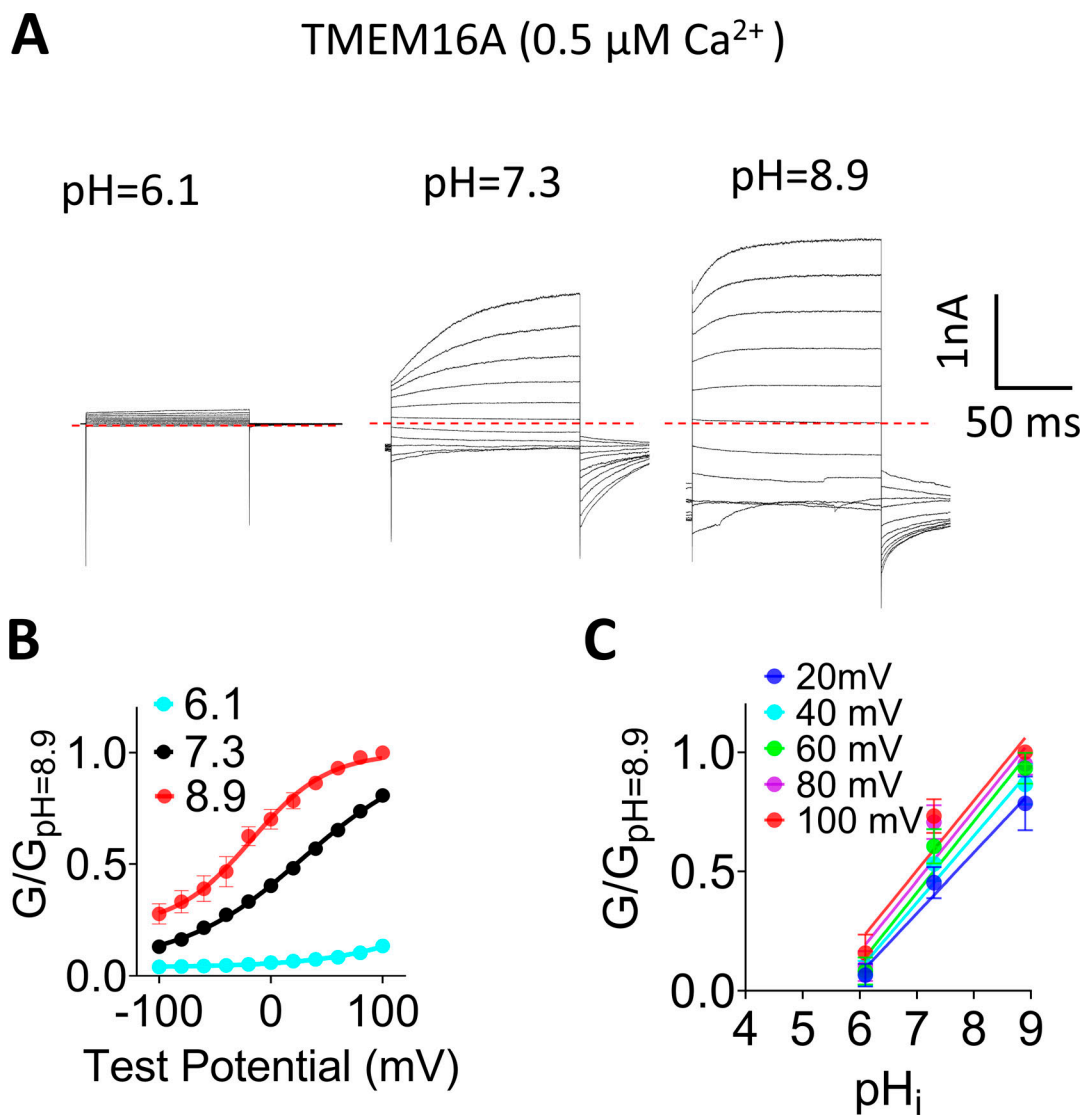
A   TMEM16A (0.5 µM Ca^{2+})

Figure S1.   **pH$_i$ regulates TMEM16A ion channel activity. (A)** Representative TMEM16A currents recorded from inside-out patches perfused with intracellular solutions containing 0.5 µM Ca^{2+} at different pH$_i$ values. Currents were elicited by voltage steps from −100 to +100 mV with 20-mV increments. The holding potential was −60 mV. All the traces shown were from the same patch. **(B)** Mean G-V relations of the TMEM16A channels under different pH$_i$ values at 0.5 µM Ca^{2+}. Relative conductance was determined by measuring the amplitude of tail currents 400 µs after repolarization to a fixed membrane potential (−60 mV). The smooth curves represent Boltzmann fits: $G/G_{max} = 1/\{1 + \exp[-ze(V - V_{1/2})/kT]\}$. G_{max} is tail current amplitude in response to depolarization to +100 mV in 0.5 µM Ca^{2+} at pH$_i$ 8.9. Error bar represents SEM ($n = 7$). **(C)** Mean conductance of TMEM16A at different pH$_i$ values was normalized to the maximum conductance at pH$_i$ 8.9 at different voltages and then plotted as a function of pH$_i$ (G-pH$_i$ relationship). Data were fitted with linear regression curves, and the mean slopes from fits were 0.27, 0.28, 0.29, 0.3, and 0.29 for 20, 40, 60, 80, and 100 mV, respectively ($n = 7$).
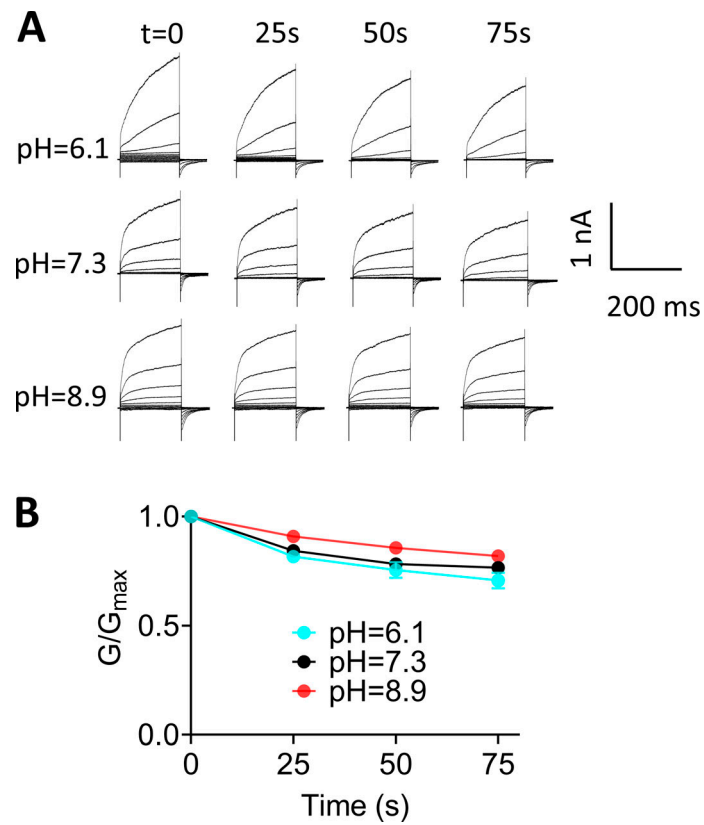
A

B

Figure S2. **Rundown of TMEM16F at different pH$_i$ values using voltage-step protocol. (A)** Representative TMEM16F currents recorded from inside-out patches perfused with intracellular solutions containing 100 μM Ca^{2+} at different pH$_i$ values. The interval between each trace was 25 s, and all the recordings were from the same patch. **(B)** Normalized conductance as different time points shown in A. Error bars represent mean ± SEM (n = 4).
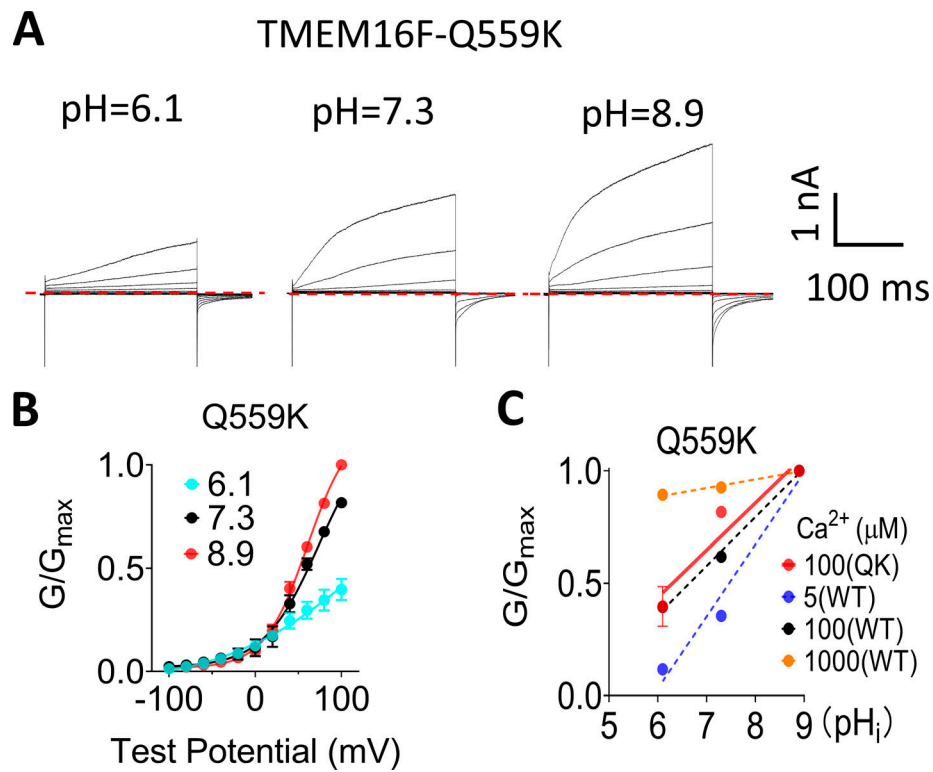
Figure S3. **Q559K, a pore lining residue mutation that eliminates channel rundown, has the same pH_i sensitivity as WT TMEM16F. (A)** Representative TMEM16F-Q559K currents recorded from inside-out patches perfused with intracellular solutions containing 100 µM Ca^{2+} at different pH_i values. **(B)** The G-V curves of Q559K currents at different pH_i values. Error bars represent SEM (n = 5). **(C)** The pH_i sensitivity of Q559K (QK) evaluated by the G-pH_i relationship. The slope of the G-pH_i relationship for Q559K at 100 µM Ca^{2+} is 0.20 ± 0.02, shown as red solid line. The G-pH_i curves of WT at different Ca^{2+} concentrations are also plotted as dashed lines for reference.
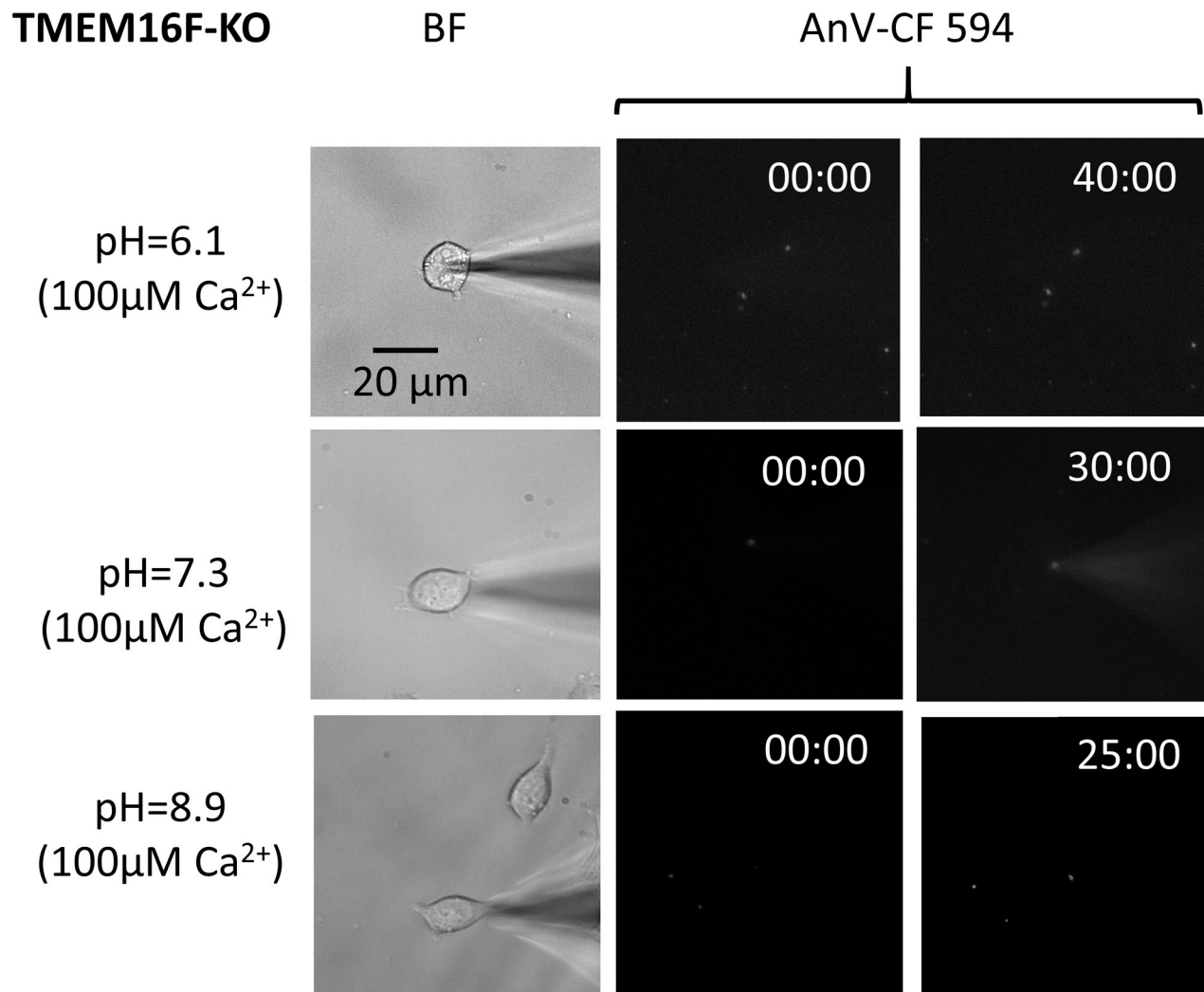
Figure S4. **TMEM16F KO HEK293T cells show no scrambling activity at all pHᵢ values tested.** Representative fluorescence intensity of AnV binding for TMEM16F-eGFP stable HEK293T and TMEM16F-KO HEK293T cells at different pH_i values (n = 4 for pH_i 8.9; n = 3 for pH_i 6.1 and 7.3). See also Video 2.
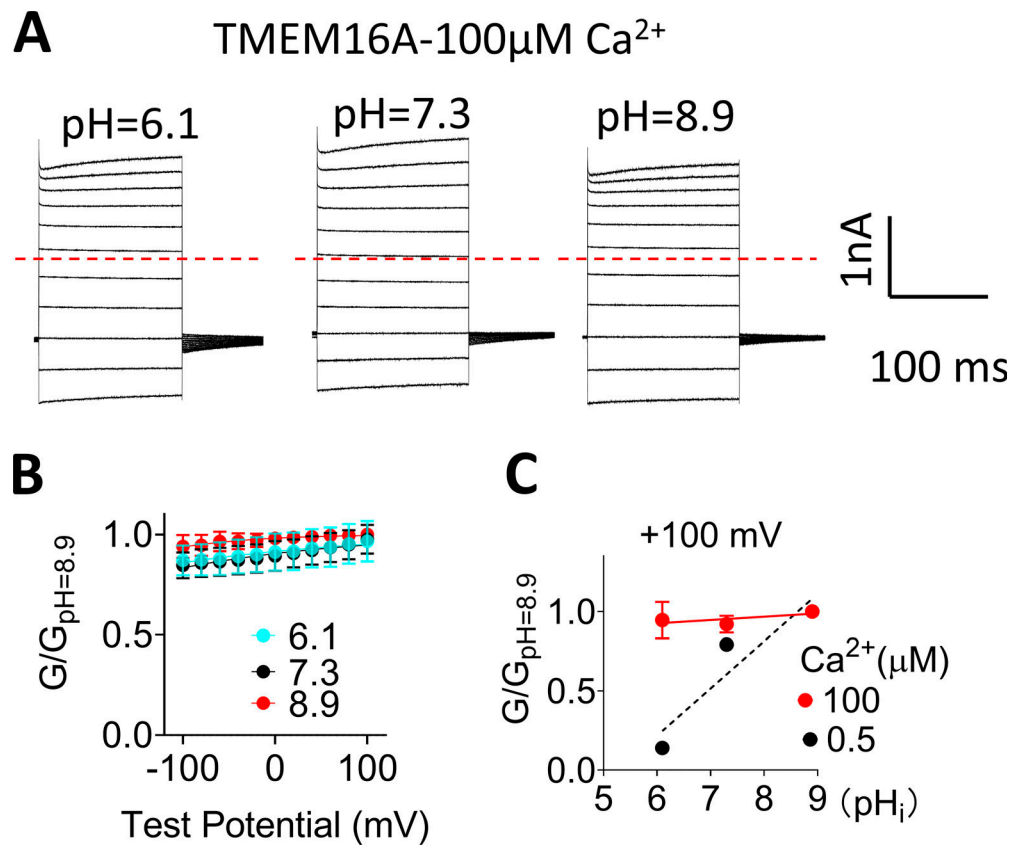
Figure S5. **TMEM16A-CaCC loses pH$_i$ regulation under saturating Ca^{2+}.** **(A)** Representative TMEM16A currents recorded from inside-out patches perfused with intracellular solutions containing 100 µM Ca^{2+} at different pH$_i$ values. **(B)** G-V relationships at different pH$_i$ values under 100 µM Ca^{2+}. All conductances were normalized to the maximum conductance at pH$_i$ 8.9 and +100 mV. Error bar represents SEM (n = 5). **(C)** *G-pH$_i$* curve of TMEM16A at 100 µM Ca^{2+} (red solid line) and 0.5 µM Ca^{2+} (black dotted line). The slopes from linear fits are 0.02 and 0.3, respectively. Error bar represents SEM (n = 5).
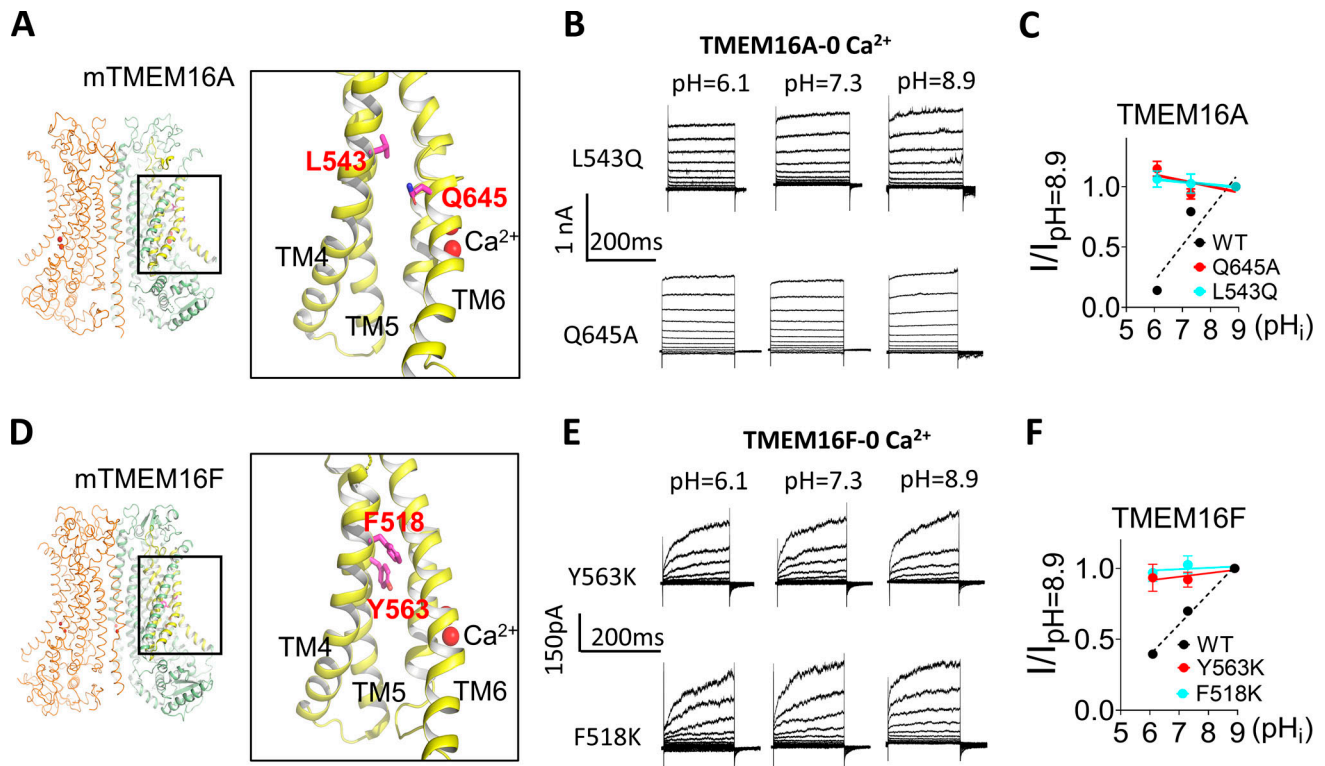
Figure S6. **pH$_i$ has no effect on the gain-of-function TMEM16A and TMEM16F mutations when Ca^{2+} is absent. (A)** Locations of L543 and Q645 on the TMEM16A structure (PDB 5OYB). The residue numbers correspond to TMEM16A (a). For TMEM16A (ac) splice variant, the residue numbers are L547 and Q649, respectively. **(B)** Representative TMEM16A-L543Q and TMEM16A-Q645A currents recorded from inside-out patches perfused with intracellular solutions containing 0 Ca^{2+} at different pH$_i$ values. **(C)** *I-pH$_i$* curve of TMEM16A mutations L543Q and Q645A at 100 mV. Slopes from linear fit for L543Q and Q645A are −0.02 and −0.04, respectively. The *G-pH$_i$* curve of WT under 0.5 µM Ca^2 was replotted as the black dashed line. Error bars represent SEM (*n* = 5). **(D)** Locations of Y563 and F518 on the TMEM16F structure (PDB 6QP6). **(E)** Representative TMEM16F-Y563K and TMEM16F-F518K currents recorded from inside-out patches perfused with intracellular solutions containing 0 Ca^{2+} at different pH$_i$ values **(F)** The *I-pH$_i$* relationship of TMEM16F mutations Y563K and F518K at 100 mV. Slopes from linear fit for Y563K and F518K are 0.03 and 0.01, respectively. *G-pH$_i$* curve of WT under 100 µM Ca^{2+} was replotted as black dashed line. Error bars represent SEM (*n* = 5). Note that the gain-of-function mutations do not have obvious tail current under 0 Ca^{2+}; therefore, *I-pH$_i$* relations not *G-pH$_i$* were plotted to evaluate their pH$_i$ sensitivities.
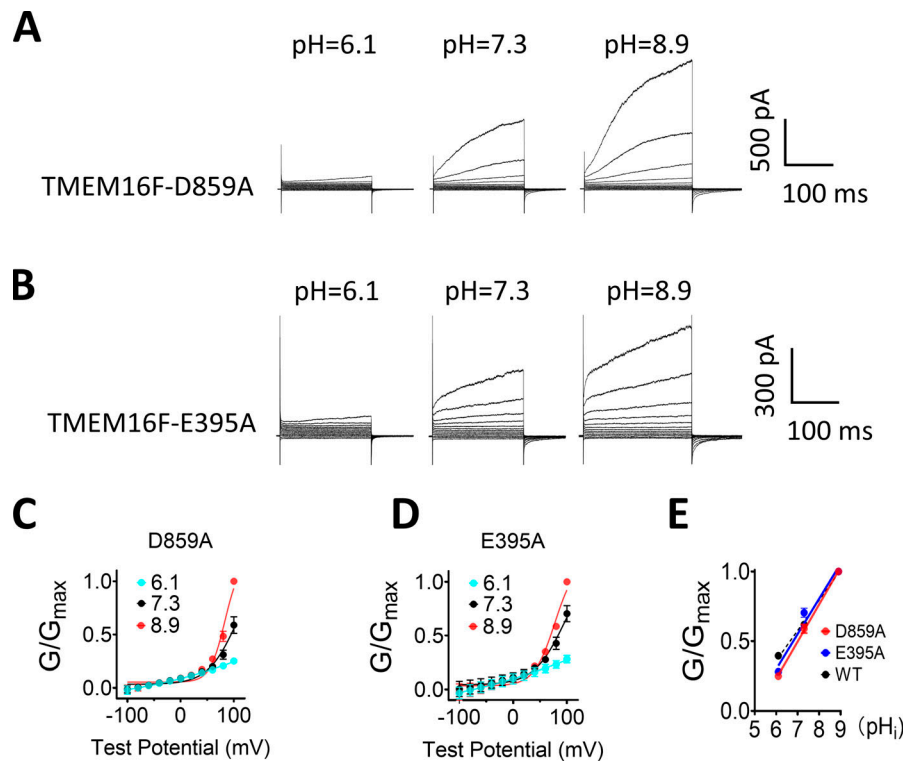
Figure S7. **Mutations of Ca²⁺ site near the dimer interface do not alter pH_i regulation on TMEM16F. (A and B)** Representative TMEM16F-D859A and TMEM16F-E395A currents recorded from inside-out patches perfused with intracellular solutions containing 100 µM Ca²⁺ at different pH_i values. **(C and D)** The G-V curves of D859A and E395A currents, respectively. Error bars represent SEM ($n = 5$). **(E)** The pH_i sensitivity of D859A (red) and E395A (blue) evaluated by the G-pH_i relationship. The G-pH_i curves of WT at different Ca²⁺ concentrations were also plotted as dashed lines (black) for reference.

Video 1. **Lipid scrambling activity of HEK293T cells overexpressing TMEM16F with 100 µM Ca²⁺ at pH_i 6.1, 7.3, and 8.9.** Related to Fig. 2 B.

Video 2. **Lipid scrambling activity of TMEM16F-KO HEK293T cells with 100 µM Ca²⁺ at varies pH_i values.** Related to Fig. S4.

Video 3. **Lipid scrambling activity of HEK293T cells overexpressing TMEM16F with 5 µM Ca²⁺ at pH_i 6.1, 7.3, and 8.9.** Related to Fig. 4 A.

Video 4. **Lipid scrambling activity of HEK cells overexpressing TMEM16F with 1,000 µM Ca²⁺ at pH_i 6.1, 7.3, and 8.9.** Related to Fig. 4 F.

Table S1 is provided as a Word file and shows the comparison of pH_i sensitivity of TMEM16F current measurements using Boltzmann and linear fits.